IOPscience iopscience.iop.org

Home Search Collections Journals About Contact us My IOPscience

# Dual-beam focused ion beam/electron microscopy processing and metrology of redeposition during ion–surface 3D interactions, from micromachining to self-organized picostructures

This article has been downloaded from IOPscience. Please scroll down to see the full text article.

2009 J. Phys.: Condens. Matter 21 224013

(http://iopscience.iop.org/0953-8984/21/22/224013)

View the table of contents for this issue, or go to the journal homepage for more

Download details:
IP Address: 129.252.86.83
The article was downloaded on 29/05/2010 at 20:00

Please note that terms and conditions apply.

IOP PUBLISHING JOURNAL OF PHYSICS: CONDENSED MATTER

J. Phys.: Condens. Matter **21** (2009) 224013 (24pp) doi:10.1088/0953-8984/21/22/224013

# Dual-beam focused ion beam/electron microscopy processing and metrology of redeposition during ion–surface 3D interactions, from micromachining to self-organized picostructures

**Warren J MoberlyChan**

Lawrence Livermore National Laboratories, CMELS, Livermore, CA, USA

Received 28 November 2008
Published 12 May 2009
Online at stacks.iop.org/JPhysCM/21/224013

**Abstract**
Focused ion beam (FIB) tools have become a mainstay for processing and metrology of small structures. In order to expand the understanding of an ion impinging a surface (Sigmund sputtering theory) to our processing of small structures, the significance of 3D boundary conditions must be realized. We consider ion erosion for patterning/lithography, and optimize yields using the angle of incidence and chemical enhancement, but we find that the critical 3D parameters are aspect ratio and redeposition. We consider focused ion beam sputtering for micromachining small holes through membranes, but we find that the critical 3D considerations are implantation and redeposition. We consider ion beam self-assembly of nanostructures, but we find that control of the redeposition by ion and/or electron beams enables the growth of nanostructures and picostructures.

(Some figures in this article are in colour only in the electronic version)

## 1. Introduction

The interaction of high energy ions with a surface produces three-dimensional changes to the surface at the nanometer scale [1–5], which in turn alter the physical interaction for subsequently impinging ions. At the macroscopic level, ion beam processing can provide uniform parameters for implantation, sputter etching, and ion-assisted deposition of thin films. This often enables the workpiece to be treated as a homogeneous two-dimensional surface, and these phenomena below, at, and above the surface are traditionally treated as separate fields of physics [6–11]. However, the introduction of boundary conditions [12, 13], including the implementation of focused ion beam tools for site-specific applications [4, 14–18], require further understanding of the ion–surface interaction in three dimensions at the nanometer scale. An earlier report [19] considers how the definition of surface has expanded to a complex 3D volume for processing at the nanometer scale and how FIB is uniting the fields of ion beam physics: implantation below the surface, sputter erosion at the surface, and ion-assisted deposition above the surface. This work focuses on ion beam phenomena 'at' the surface: surface erosion, sputtering, machining, and self-organization [2, 8, 20–23]. However, the physical interactions below and above the surface are encroaching into the FIB etching process: nanomachining is controlled by implantation theory; and the reverse reaction of deposition is controlled during erosion to grow picostructures.

By the nature of site-specificity (scanning or patterning) of a focused ion beam [4, 24], the surface is no longer expected to be two-dimensionally isotropic. But in fact, even when a broad static ion beam impinges a material, the surface loses its planarity. Sigmund sputtering theory explains the surface roughening process [1, 8]; and Bradley and Harper expand to show control of such roughening process [25], thereby opening research venues for self-organized nanostructures [2, 5, 26–29]. Each individual ion,

 © 2009 IOP Publishing Ltd Printed in the UK

independent of whether it is in a FIB digitally patterning at gigahertz and nanometer pixels or in a broad static beam exposing a full wafer, is affected by 3D surface changes enacted by earlier impinging ions. An important parameter for ion erosion is yield—number of atoms removed for each impinging ion; and in a steady state condition, the ion etch rate could be a constant. For a FIB tool, the spatial resolution of sputter etching is equally important, and could have an ultimate resolution limit of the ion sputter interaction, nominally calculated by SRIM as ∼1 nm for 30 keV ions [30–32, 19]. However, the sputter yield at any given pixel on a 3D surface changes due to events occurring at nearby 3D voxels both before and after. Furthermore, as desired structures are reduced to nanometer scale, the resolution limit for FIB processing increases from the traditional 1 nm on a 2D surface to a cascade volume of ∼20–30 nm calculated from implant theory [31, 32]. Although the modern FIB can expeditiously input a high current into a small volume of the workpiece, sputter theory models each impinging ion as a discrete separate event. However, when considering the expansive cascade volume, FIBs are approaching temporal overlap between impacting ions (tens of picoseconds). Even in atomistic models, the engineering parameters critical to ion beam micromachining and processing of nanostructures become aspect ratio and redeposition.

All surface modulations develop a 3D aspect to them whether processed with a static big ion beam or a scanning FIB, and the subsequent changes to already developed 3D surfaces can occur independent of whether the ion beam is larger than the surface features or is a smaller beam that is scanned over a larger area [5, 12, 19]. All surface modulations may be modeled as pits (trenches) or holes, and experiments in this paper distinctly define a pit as having a bottom and a hole as penetrating through a membrane. The ion beam processing of both pits and holes, whether between waves of ripples or as singular apertures, are dominated by their aspect ratio [33]. Ion sputter theory often includes SRIM/TRIM calculations [31], but boundary conditions are paramount to describing when a pit becomes a hole. As pits, holes, and membrane thickness scale smaller and closer, additional geometric conditions of the sputtering theory need to be defined: topside, bottomside, frontside, backside. A pit deepens by topside (or top-down) sputtering, albeit with ever decreasing yield due to topside redeposition as its aspect ratio increases. But as the pit becomes a hole, the residual membrane is so thin that ions pass through and sputter the bottomside with the hole forming bottom-up. Bottomside sputter often has much greater yield than does topside sputter. Two-step processing further allows for two different angles of ion inclination and/or pre-patterned variations in boundary conditions [5, 20]. A membrane with a hole or pit may be turned over and exposed to erosion from the backside with different response than if further eroded from the initial frontside. Generically, the energy of an incident ion may be chosen such that it will interact with atoms nearest to the top surface and thus provide the most efficient ion sputter etch yields. Hobler *et al* [32, 19] has noted that the surface interaction area for sputtering is ∼1 nm, which predicts further improvement from present FIB resolution of 4–5 nm even though the 30 keV ions in tools evoke substantial energy spread below the surface. TRIM calculations [32, 19] predict a worse resolution of 5–20 nm for FIB as an implant tool, but other than subsurface damage such as defects or amorphitization, the resolution of sputtering initially appears superior. However, once three-dimensional geometries are considered, this energy spread also delocalizes the sputter etching process such that practical small shapes machined by FIB become more limited by considerations of the implant theory. Attempts to process high aspect ratio nanostructures in close proximity may find the ion beam performing topside sputter on the frontside of one structure, while also exposing another structure to backside erosion and/or cause bottomside sputter. The 3D boundary conditions although complex, produce extremely reproducible and easily controlled geometries of high aspect ratio (10%–1000%), and FIB can apply such shape site specifically, with the important controlling parameter being: redeposition.

Pits and holes have a developing shape, as well as diameter, depth, and location. Thus metrology of ion beam processing requires spatially discerning techniques provided by electron microscopy. The dual-beam FIB/SEM (focused ion beam/scanning electron microscope) provides natural *in situ* diagnostics; however, *ex situ* TEM (transmission electron microscopy) provides additional resolution to quantify size and orientation of subnanometer ripples and assess third dimensions such as membrane thicknesses for pits not yet becoming holes and for holes having re-evolved to pits. However, images provided by TEM, SEM, and FIB require analysis of complex contrast mechanisms, and imaging can even input sufficient energy to alter surfaces. Thus imaging experiments require controlled acquisition parameters [33, 34]. Imaging can provide end-point detection [35, 36] to establish when a pit becomes a hole through a membrane; however, the contrast is evaluated differently for different workpieces. Electron microscopy tilting techniques have been developed to evaluate parameters of aspect ratio and redeposition [33]. The increasing aspect ratio as a pit deepens leads to redeposition within the pit [37]. Redeposition is a quantified detriment to yields, and more so to enhanced yields, when machining a micron-scale pit. Redeposition inside nanometer-scale holes can control their shrinkage; or bottomside redeposition inside a pit during backside exposure can grow and encapsulate 3D arrays of nanometer dots; or redeposition inside the nanometer-scale pits between ripples can lead to ripple growth [25, 33]. And at the picometer scale, the reverse reaction of deposition itself can become the end product of the erosion process, as well as the converse of erosion during deposition.

## 2. Experimental results and discussions

Experimental results are presented in 3 parts: the production tool use of ion beam erosion to etch a material is applied by quantifying yield (number of atoms etched off for each ion impinging the surface) and by methods to enhance yield. Diamond is the material studied, as FIB etching of carbon-based materials is slow and enhanced yield is desirable [38, 39]. Also FIB provides a fast and efficient

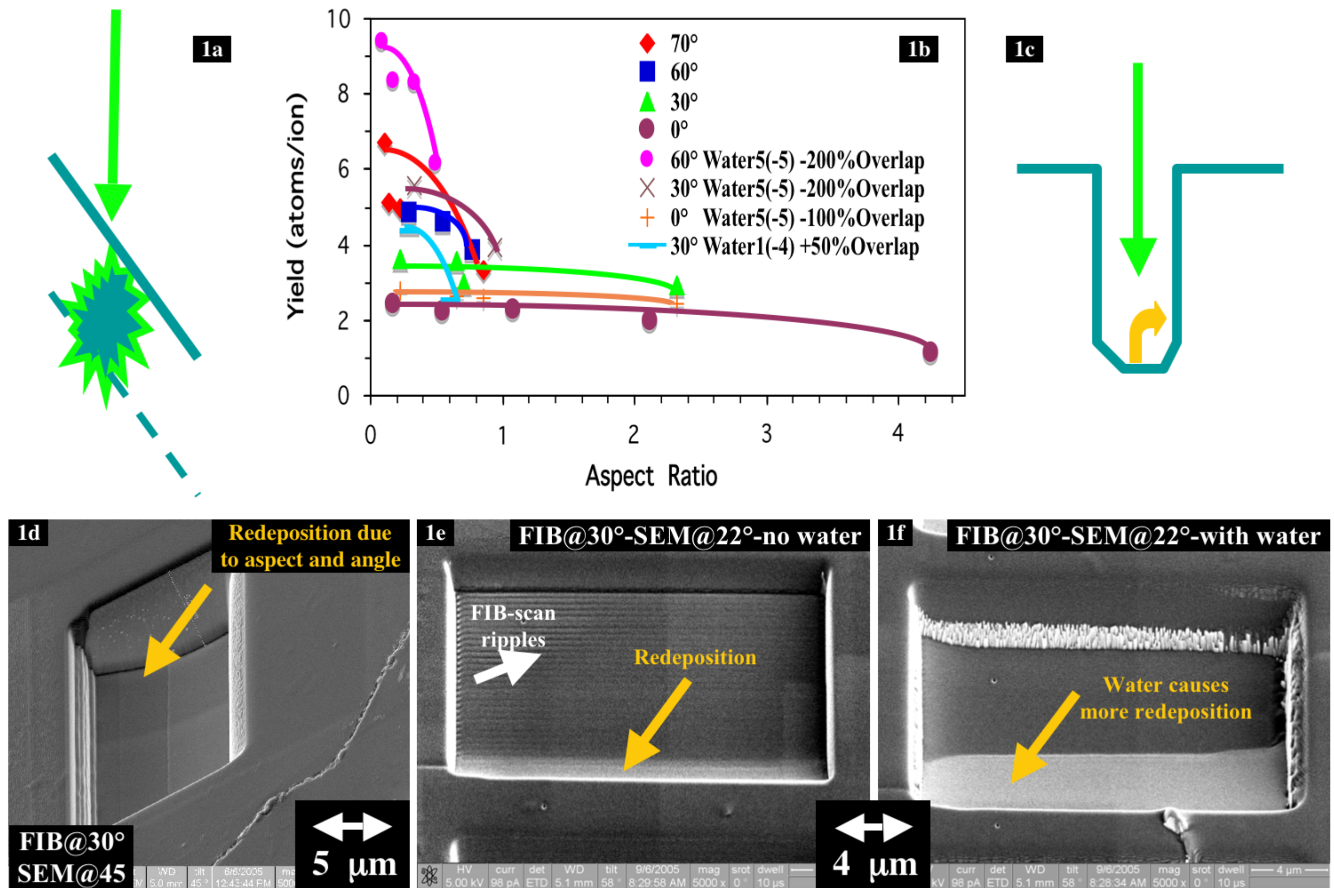


**Figure 1.** (a) From Sigmund sputtering theory [1], an ion beam incident onto a surface at an angle (non-normal) imparts more energy closer to the surface, thereby enhancing the sputtering yield: # atoms off per ion in. (b) Chemistry can also enhance yield (water vapor helps diamond etch [39]); however, yield enhancers more adversely deteriorate with aspect ratio [33]. (c) As a pit deepens, sputtered material less easily escapes and redeposition increases. (d) Redeposition increases with angle and aspect ratio, becoming visible in SEM of micron-scale pits; and is more prevalent in nanoscale topologies. ((e), (f)) Redeposition increases with added chemical enhancers. In order to activate chemical enhancement, the ion beam current must be lessened, scan dwell time minimized (ideally $\ll$1 ns), and gaps imposed in the scan pattern. This later 'negative overlap' manifests as FIB scan lines in the etched surface (e), which become mitigated (f) in the presence of chemical vapor that defocuses the ion beam spot size. FIB and SEM tilts are orthogonal in (d) and parallel in ((e), (f)). FIB can drill additional small pits ((e), (f)) for metrology [33].

means for studying materials processing, consumes little of expensive/rare materials (such as diamond), produces minimal quantities of waste, and enables safe, contained handling as desired for hazardous materials. Secondly, all ion beam processing involves 3D shapes at the nanometer scale. An aspiring shape, albeit of simple geometry, is to make a nanometer-scale aperture by ion beam micromachining or drilling [40–43]; however, practice has shown that closing a hole can make it even smaller [5, 36]. Amorphous silicon nitride membranes are studied because of their robust and pertinent relevance to Si wafer technologies such as MEMS and also to allow modeling comparisons to ignore complex crystalline-ion-channeling effects [44]. And finally, the ion erosion process can be optimized to self-organized topologies [25, 45–49], with these ripples becoming potential templates for nanostructures, or to direct-write picostructures [50] when controlling deposition during erosion, or to grow nanometer-scale topologies on top of pedestals when controlling erosion during depositions [34]. Again diamond and carbon-based CVD structures are studied in the third part because of the well-controlled ripples formed during room temperature processing, however, the reverse reaction processes are similarly optimized for other materials as well as other incident ion species.

### 2.1. *Yield depends on aspect and redeposition*

The FIB enables site-specific sputter etching [4], and also provides high current densities to tailor sets of nanometer-scale structures in minutes with doses exceeding $1 \times 10^{19}$ ions $cm^{-2}$. Still the FIB does not etch fast enough and thus methods to enhance yield are imposed as similar for big static beam processes. Yield is enhanced by increasing the ion beam angle of incidence [39]. (Normal is defined as 0°). Sigmund [1] showed grazing incidence inputs more energy closer to the surface and thus increases sputtering efficiency (figure 1(a)). In order to sputter etch an atom away from the top of most surfaces, the incoming ion need not be >1 keV (SRIM calculations) [31]. Even though over-voltage implants the

average ion many atomic planes below the surface, it still enhances the effective sputtering yield (number of atoms getting off the surface per ion incident). The state-of-the-art FIB has therefore chosen a 30 kV Ga ion because it is most efficient for fast etching of many materials (and especially Si), as well as the practical ion column issues of the higher kV being able to produce a higher current density (1–20 000 pA) to a smaller focused spot (4–500 nm) [4]. When a single 30 kV Ga ion inputs its energy, modeling [3, 10, 30, 31, 51, 52] indicates thousands of atoms undergo displacements, but these are all subsurface and FIB yields remain modest; ∼4 for silicon, ∼2 for diamond [4, 39, 53]. However, when ions impinge at higher angles of incidence, the yield enhancements of these over-voltage ion beams are even more dramatic.

Still the FIB does not ion etch fast enough, thus chemical methods are commonly imposed to enhance yield. Noting that ion beam etching occurs in a vacuum, the options for chemical enhancement must be modest and compatible with the entire processing system/sample. In some cases chemistry can be fairly benign. As an example, the addition of simple water vapor can enhance the yield for diamond 10-fold, with Adams *et al* [39] providing a graph of yield enhancement as a function of angle of incidence and water vapor. In such cases, the chemistry becomes adsorbed on the top surface and alters the bonding condition of the topmost atomic layer. This in turn enables the incident ion energy to more efficiently break the chemical bonds of the top layer away from the remaining substrate. Also the released atoms (and molecules) should have a high vapor pressure and a low sticking coefficient to ensure their easy removal and minimized redeposition. However, the limitation of chemical enhancement for FIB requires the next layer of chemical enhancement reaction to occur before the next incoming ion. During the processing of small-scale geometries with modern high-current-density FIBs, the arrival of the next ion has much higher probability than the arrival of the next reacting gas molecule. In order to accomplish chemical-enhanced ion etching on diamond, the ion dose rate had to be reduced more than ten-fold and dose per pixel dwell reduced to $<1 \times 10^{12}$ ions $cm^{-2}$. Otherwise, the sputter yield for diamond was actually reduced by the addition of water vapor at higher current densities [33], partly as a consequence of the increased scatter enacted upon the incoming ion beam by the excess vapor pressure (locally upwards of $10^{-3}$ Torr), but also due to increased redeposition in the presence of (locally) poor vacuum. The minimum dwell time at a pixel in a modern FIB tool is ∼100 ns. If/when dwell control is reduced to picosecond scale, then the current can be increased and designed patterns can still accomplish chemical-enhanced etching.

The FIB offers many digital engineering controls; pixel size and dwell time, scan pattern including overlap, current, and spot size. The yield enhanced by chemistry and by angle of incidence require an optimization of these engineering controls, especially judicious negative overlaps [33]. Once the etch rate is enhanced, it becomes possible to consider additional geometrical effects on yield imposed by boundary conditions common to FIB processing [33, 37]. In particular, the site-specific high current enacted by FIB patterning leads to production of 'pits' (three-dimensional shapes) in the surface. Any surface topology can be modeled as a set of pits or trenches in a surface, and the ion–surface response may be similar for a beam infinitely larger than the pit as for a beam focused much smaller but then scanned over a larger area. When the ion sputter etches at the bottom of a pit, then the yield becomes a function of the aspect ratio of the pit [33, 37, 54]. Yield drops as a function of aspect ratio, and figure 1(b) shows such drop is more pronounced when the yield has been enhanced by either angle of incidence and/or chemistry. Aspect ratio has been defined as depth over width of a trench; and any further increase in the length of the trench provides no assistance to increasing yield [33]. In the schematic of figure 1(c), there is difficulty for sputtered species to escape the bottom of the pit and subsequent etch rates decrease. Surprisingly, this deterioration of yield starts to be significant even when the aspect is only 10% (see figure 1(b) [33]). SEM imaging (figure 1(d)) depicts a region of material building up at the downstream edge of this FIB pit etched at an angle of inclination of 30° (from right to left). The amorphous nature of (most) redeposited material can provide a different imaging contrast from the base substrate; thus the redeposition build-up is visibly brighter at the leading (bottom) edge of the two etch pits viewed in figures 1(e) and (f). The addition of water vapor does enhance yield to produce a deeper pit (figure 1(f)), however, it also enhances the redeposition effect. Excess vapor pressure can cause more scatter of the sputtered species attempting to escape from the pit, leading to an increase in redeposition with aspect ratio. Figure 1(e) depicts horizontal lines that arise from an intentional gap patterned between pixels. The negative 200% overlap is a necessary engineering application [33] to accomplish chemically enhanced yields in modern FIBs with their high current density probes. When no water vapor is added, such gaps in patterning impose a patterned roughness to the etched surface, but with negligible change to overall yield. (Negative overlap is applied in both orthogonal directions, but vertical gaps are mitigated by scan pattern/speed. Excessive intentional surface roughness does diminish yield.) However, this computer-patterned roughness does not manifest in the chemically enhanced process (figure 1(f)), because the lower current in beam tails are relatively more enhanced by chemistry [33], and because the excess water vapor can also defocus the incoming ion beam.

The FIB can process small three-dimensional structures, and more importantly direct-write, site specifically, such structures. Although angle of incidence and chemistry can enhance yield, in practice most FIB processing is faster, as well as more precise and easier to engineer controls, when the FIB is normal to the workpiece. When a surface is inclined, the projected current density per surface area is reduced more than the yield is enhanced. I.e. a 1 $\mu$m deep small pit is etched quickest with a normal FIB; and the high current density probe etches quicker than the low ion beam flux required for chemical enhancement [33]. Normal incidence also more readily achieves aspect ratio, as well as vertical sidewalls and precise edge definition. Grazing incidence does increase yield (per ion), but early models akin to crystal dissolution can be misleading when applied to the practice of

FIB nanostructuring. Barber *et al* [55] and Carter *et al* [56] plot erosion slowness due to varying angle of incidence on curved surfaces. In practice, however, the projected current density drops with grazing angle; thus FIB cutting of 7 $\mu$m-diameter carbon-based fibers etches the normal surface faster than the sides [57, 50]. (FIB etching of small diameter fibers allow all angles of incidence to simultaneously develop self-organizing topologies that match varying FIB angle onto a flat surface; rough surfaces are smoothened by normal incidence, and 1D ripples and 2D steps form at grazing incidence. See section 2.3 and [39].)

Barber's model [55] also has deeper troughs developing steeper sidewalls and shallow troughs developing sloped sidewalls; but when a scanning FIB processes trenches of high aspect ratio, the sidewalls become more sloped as the trench deepens. Orthogonal trenches of modest depth with perfectly vertical sidewalls can be patterned into most materials by scanning FIB (e.g. figure 5 of [33]). However, the extended beam tails of a FIB, especially in static processing mode, become dominant to cause higher aspect ratio sidewalls to slope. Barber's experiments [55], which apply a static ion beam at a fixed inclined angle to a rotating, dimpled surface (e.g. TEM sample preparation), also observed two self-organizing features that can be produced by FIB, but for different reasons. Barber attributes cones to pre-existing defects, but modern defect-free crystals can develop cones during TEM sample preparation or dots change to cones as a result of a change in grain orientation (see figure 5(d) of [37]). Barber attributes a change from 2D dot topology to 1D ripples as due to the distance from the axis of rotation. However, TEM sample preparation commonly develops different topologies at different angles on the same sample [58]. FIB sample processing can produce more uniform topologies than a static beam (see section 2.3), but FIB also shows topology changes due to boundary conditions such as nearby grain boundaries (see figure 5(a) of [37]), interfaces between cross-sectioned layers [37], and pre-patterned lines [12]. The computer control of a well-aligned FIB achieves wonderfully precise small shapes, but the effects of aspect ratio on yield remain the same for each individual ion in Barber's rotating static ion beam as for the scanning FIB.

The difficulty of getting material out of a deep pit appears a simple but reasonable concern [54, 59]. As the yield is dropping in figure 1(b), what is increasing? Redeposition is increasing. In a macroscopic kinetic reaction, redeposition may be incorporated as a source term of deposition [60] countering erosion. However, the FIB etches micro-craters, and redeposition also serves as a well-controlled source term countering sputter yield at the micron scale. It becomes a justifiable expectation (in parts B and C) that nanometer-scale modulations can be modeled as pits of aspect ratio, which as they grow will experience redeposition within themselves [25, 33, 49]. If redeposition occurs in a micron-size pit due to aspect ratio, then a nanometer-scale pit such as a ripple has redeposition occurring in it, too. Thus, redeposition also becomes a source term for ripple growth. When ripples self-organize over the macroscale, then redeposition again becomes a macroscopic kinetic term.

### *2.2. FIB processing and metrology of holes through membranes; aspect ratio and redeposition on the backside*

Although modern FIBs have high current density ion beams that can provide local dose rates in excess of $1 \times 10^{20}$ ions cm$^{-2}$ s$^{-1}$, it remains impractical to consider serially scanning FIB for production of most MEMs structures. Removal of $\sim$1 $\mu$m$^3$ of Si per second is a practical limit for most geometrical features; removal of 1 mm$^3$ of material between MEMS would take 30 years. Since a FIB can etch a small pit, it is often requested to etch a hole through a membrane to provide an aperture or site-specific filter, such as may be used for sequencing DNA [5, 36, 61]. However, incorporating a single $\sim$1 nm hole with Si technology would require a hole through a nominally 500 $\mu$m thick wafer, which because of the aforementioned aspect ratio concern would require the top diameter of the hole to be upwards of 100 $\mu$m, >1 million cubic microns removal, and >2 weeks of FIB processing. However, FIB processing as only one component of MEMs processing might require only seconds. Figure 2(a) is a low magnification SEM image depicting large (>100 $\mu$m) vias that have been chemically etched through a Si wafer. A CVD silicon nitride film had been deposited on the opposite side of the Si wafer and this film persists after chemical etch as a membrane at the bottom of the via. The silicon nitride membrane appears dark in figure 2(b), as imaged by the few secondary electrons emitted while scanning the FIB beam. The FIB can then cut a hole through the thin membrane in seconds. However, poor secondary emission from the bottom of a via not only makes the membrane appear black, but also makes it difficult to establish when the hole has perforated the membrane. In order to prevent overetching from eroding the hole too big, end-point detection is necessary when etching holes. In this case, the Si wafer and membranes are supported many millimeters above a metallic substrate, and the FIB ions penetrate through the hole and then impact the metal to generate many secondary electrons. Thus the hole appears bright. Figure 2(c) is a higher magnification image of a 1 $\mu$m diameter hole etched through a $\sim$20 nm thick silicon nitride membrane, with nanometer-scale precision and a total process time <5 s.

*2.2.1. Array processing of pits and holes through 400 nm thick membranes.* This same procedure of hole etching and end-point detection is used to make arrays of small holes through 400 nm thick membranes as imaged by SEM, FIB and TEM in figures 2(d)–(f), respectively. Computer patterning provides a variation in diameters (controlled to be nominally 100, 60, 50, 30, and 25 nm for columns 1 through 5, respectively) as well as 'depths' listed in table 1. Depth is achieved by the duration of etching time with the FIB computer considering a constant etch rate. Since yield decays with aspect ratio, the etch rate of silicon nitride was established for a large hole with an aspect ratio <10%. Although all depths, ranging from 1000 to 20 000 nm should represent conditions of 'overetching' through the 400 nm thick silicon nitride, the decayed yield due to aspect ratio leads to some holes not penetrating the membrane. Once the FIB etching

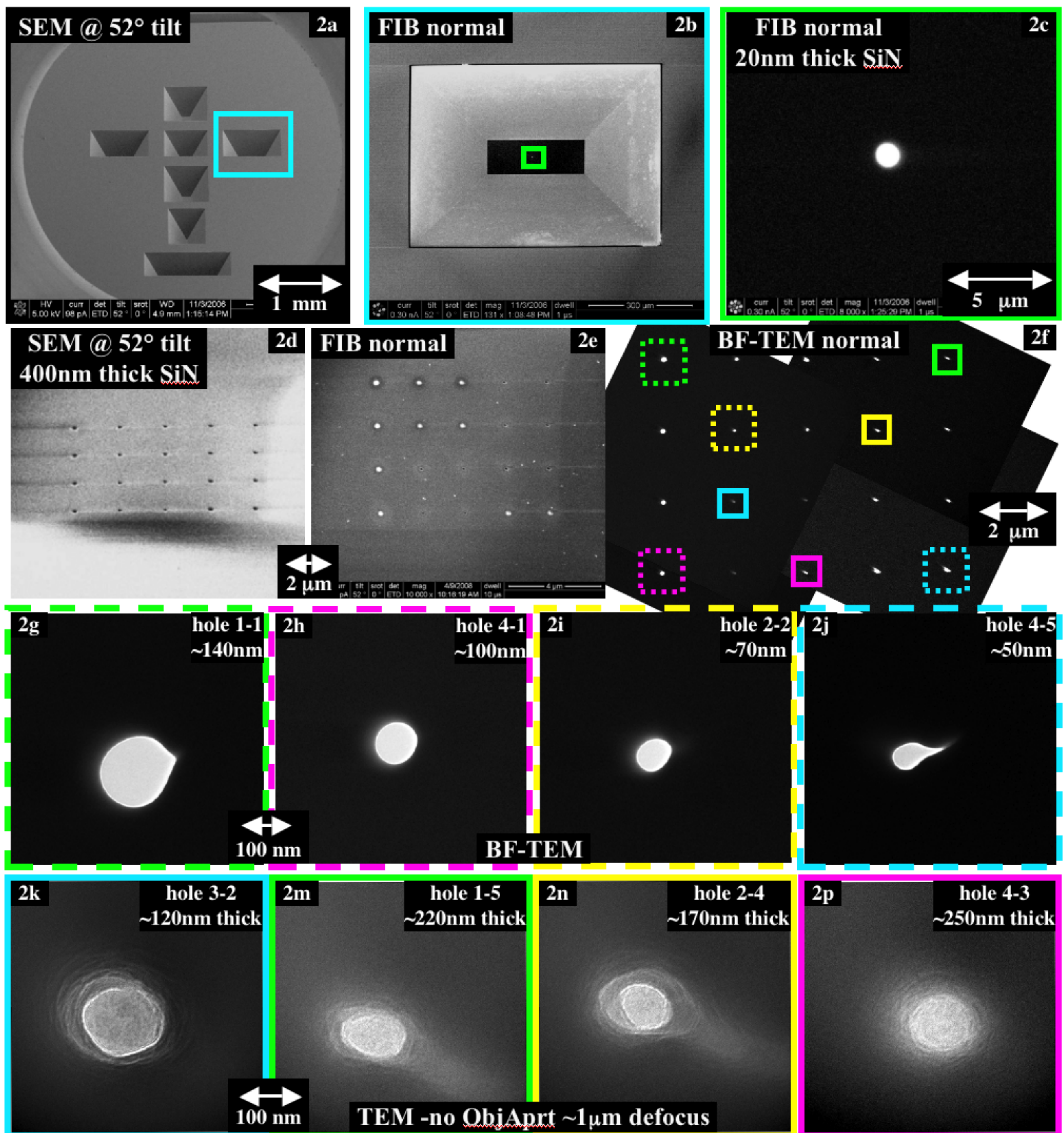


**Figure 2.** (a) SEM image of vias patterned through Si wafer by chemical etching. (b) Secondary electron image generated by FIB depicts SiN membrane that appears dark and covers the bottom of the via. (c) Higher magnification FIB image after FIB-processed aperture through membrane in ∼5 s. 30 keV ions passing through hole impinge a metal surface several mm beyond, exciting many secondary electrons, and enables hole to be 'visibly bright' for end-point-detection. (d) SEM image of surface of ∼400 nm thick SiN membrane after FIB etching array of holes. (e) Same array of holes imaged with FIB normal. Secondary electron contrast is complex. FIB ions passing through open holes excite many secondary electrons when impinging metal surface far beyond. However, surface topologies at the top rims of holes also lead to typical brightness of secondary emission. Many bright particles are also observed on the top surface, presumably being deposited due to the complex charge distribution during processing a nonconductive material. 'Charging' is evident in the SEM image, and charging during FIB processing can smear precision upwards of 1–2 $\mu$m. Thus in order to pattern the array of holes, the sample was exposed to a flood of electrons simultaneous to the FIB patterning. (f) Bright Field TEM image (montage) of the same array of holes. Although SiN membrane appears black in captured low magnification image, sufficient electrons transmit such that differential charging during image capture is not problematic. The normalized intensity can establish the thickness of residual membrane in those holes of the array, which do not fully penetrate. ((g)–(j)) Higher magnification BF-TEM images of 4 fully penetrating holes, and ((k)–(p)) TEM of 4 pits with residual membranes acquired without objective aperture and 1–2 $\mu$m of defocus to provide extra phase contrast for image capture. Transmission intensity is used to quantify membrane thickness (see table 1).

**Table 1.** Array of holes processed through 400 nm thick amorphous SiN membrane. After patterning, holes are exposed to further erosion over the entire area of the array, frontside, backside, and/or by near-field (o-ring) erosion. '*d*' represents diameter of opening of penetrating 'holes' as measured by TEM. '*t*' represents thickness of membrane remaining in 'pits' that did not perforate (or were subsequently closed). Membrane thicknesses are measured relatively, by absorption of TEM intensity. The intensities vary $<\pm1\%$ due to beam stability, $<\pm5\%$ due to variations in film thickness, and $<\pm5\%$ due to counting and measurement statistics. Initial diameters are based on patterning (overetching erodes to larger diameters and underetching can be smaller). Depths are based on calibrated SiN etch rate, and all are in excess of the ~400 nm membrane thickness. All holes close upon exposure; however, similar processing to array of holes in thin (20 nm) membrane had all holes open upon exposure.

| Hole | Patterned diameter (nm) | Effective depth (nm) | As-processed | 20 nm frontside erosion | 40 nm frontside erosion | 20 nm backside erosion | 40 nm backside erosion | 100 nm backside erosion | 10 nm-o-ring (after 40 nm eroded) |
|---|---|---|---|---|---|---|---|---|---|
| Hole 1–1 | 100 | 5 000 | 150-*d* | 135-*d* | 95-*d* | 125-*d* | 130-*d* | 130-*d* | |
| Hole 1–2 | 60 | 5 000 | 85-*d* | 80-*d* | 40-*t* | 60-*d* | 30-*d* | 50-*t* | |
| Hole 1–3 | 50 | 5 000 | 60-*d* | 45-*d* | 50-*t* | 65-*t* | 50-*t* | 200-*t* | |
| Hole 1–4 | 30 | 5 000 | 200-*t* | 250-*t* | 250-*t* | 270-*t* | 50-*t* | 200-*t* | |
| Hole 1–5 | 25 | 5 000 | 220-*t* | 250-*t* | 260-*t* | 280-*t* | | 220-*t* | |
| Hole 2–1 | 100 | 3 000 | 125-*d* | 120-*d* | | 110-*d* | 120-*d* | | |
| Hole 2–2 | 60 | 3 000 | 70-*d* | 55-*d* | 60-*t* | 9-*d* | 40-*d* | 110-*t* | |
| Hole 2–3 | 50 | 6 000 | 60-*d* | 60-*d* | 70-*t* | 25-*d* | 30-*t* | 40-*t* | |
| Hole 2–4 | 30 | 6 000 | 170-*t* | 280-*t* | 240-*t* | 230-*t* | 170-*t* | 170-*t* | |
| Hole 2–5 | 25 | 6 000 | 200-*t* | 250-*t* | 260-*t* | 270-*t* | 210-*t* | 210-*t* | |
| Hole 3–1 | 100 | 2 000 | 115-*d* | 110-*d* | | 100-*d* | 105-*d* | | |
| Hole 3–2 | 60 | 2 000 | 120-*t* | 130-*t* | 150-*t* | 140-*t* | 50-*t* | 60-*t* | |
| Hole 3–3 | 50 | 2 000 | 190-*t* | 220-*t* | 220-*t* | 210-*t* | 160-*t* | 160-*t* | |
| Hole 3–4 | 30 | 10 000 | 45-*d* | | 160-*t* | | 110-*t* | 150-*t* | |
| Hole 3–5 | 25 | 10 000 | 120-*t* | 200-*t* | 220-*t* | | 130-*t* | 150-*t* | |
| Hole 4–1 | 100 | 1 000 | 100-*d* | 75-*d* | 50-*t* | 65-*d* | 65-*d* | 30-*t* | 40-*d* |
| Hole 4–2 | 60 | 1 000 | 190-*t* | 260-*t* | 230-*t* | 230-*t* | | 150-*t* | |
| Hole 4–3 | 50 | 1 000 | 250-*t* | 280-*t* | 280-*t* | 280-*t* | 220-*t* | 220-*t* | |
| Hole 4–4 | 30 | 20 000 | 75-*d* | 35-*d* | 65-*t* | 60-*t* | 20-*t* | 50-*t* | |
| Hole 4–5 | 25 | 20 000 | 50-*d* | | 100-*t* | 70-*t* | 40-*t* | 50-*t* | |

does penetrate the membrane, however, the tails of the ion beam spreading beyond the Gaussian distribution act to ream and erode the hole to a larger diameter. Holes (or pits) eroding due to beam tails initially develop sloping sidewalls, the angles of which invoke a higher yield (per figure 1(a)). Even though the ion beam tails have a lower current density compared to the Gaussian peak, the peak is attempting to etch at the bottom of the pit and provides lowered yield due to aspect ratio. The beam tails, on the other hand, are acting with enhanced yield at the tops of sloping sidewalls. Thus at the geometrical condition of a deep pit, the weak beam tails can etch as fast as the intense Gaussian peak. Eventually once the hole penetrates the membrane, further beam-tail-erosion will remove slope and actually sharpen the sidewalls. As noted in section 2.1, modeling of ion beam erosion predicts more sidewall slope for shallow pits and steeper sidewalls for higher aspect ratio [55]. However, the scanning FIB can easily process precise vertical sidewalls in pits of modest depth (see figure 5 of [33]). Yet when processing small, deep pits, the FIB beam tails dominate at high aspect ratios to slope the sidewalls. Only upon hole penetration do beam tails ream the hole back to vertical sidewalls. The holes in column 1 range from 100 to 140 nm diameter as a consequence of overetching, with TEM imaging providing metrology of holes 1–1 and 4–1 in figures 2(g) and (h), respectively.

SEM imaging is achieved with a 5 kV incident electron beam at an angle of 52° and the holes appear darker due to lower secondary emission. The nonconductive nature of the silicon nitride causes a dramatic charging contrast and even a smearing effect as the SEM scan pattern passes the array of holes in figure 2(d). Also, just as ion emission out of a pit is diminished, the low secondary electron emission precludes 'seeing' how deep pits are. This is true even when SEM images normal to a surface, which can then preclude any detection of holes or pits as rim contrast is lessened. Rather, the 'darkness' of a small pit/hole imaged by SEM becomes a complex combination of the pit depth, the diameter, and the slope of rims (as well as potential charging artifacts affecting local contrast). Most holes exhibit comparable diameter by SEM because of beam-tail erosion at their top rims, however holes 3–2, 3–3, 4–2, and 4–3 do appear 'smaller' in figure 2(d) as a consequence of substantially lower total dose exposure. Unlike FIB, SEM incident electrons easily penetrate these membranes, thus an end-point detection mechanism is less reliable for SEM imaging.

FIB imaging at 30 keV normal to the hole array produces a complex combination of secondary electron contrast. FIB ions passing through open holes excite many secondary electrons when impinging a metal surface far beyond, thus perforated holes are bright. However, inclined surface topologies at the top edge of all holes (and pits) lead to a typical ring of brightness of secondary electron emission, even for those holes that do not fully penetrate the membrane. Also many bright particles are observed on the top surface, presumably being deposited due to the complex charge distribution during the array processing of a nonconductive material. Charging during

FIB processing can smear precision upwards of 2 $\mu$m even with the low current used for this FIB processing. Thus in order to FIB pattern the array of holes using positive Ga ions, the sample was simultaneously exposed to a flood of electrons with a dose rate of $\sim 1 \times 10^{14}$ ions cm$^{-2}$ s$^{-1}$. The gray level of the background in FIB image of figure 2(e) is due primarily to secondary emission from the top surface, and penetration of the ion beam through the 400 nm thick membrane should be a negligible component of imaging. Inside pits which do not fully perforate, the remaining membrane stops FIB penetration, and also the depth of the pit prevents secondary electrons from escaping from the top. Thus the image appears darkest inside these non-perforating holes (pits).

TEM imaging is performed with a 300 keV-FEI-CM300F and Gatan GIF300-2kCCD, with low magnification images ($\sim$5000$\times$ montage of figure 2(f)) acquired in bright field mode and with intensity normalized to 10 000 counts per second. This enables the open holes to appear bright (10 000 counts) and the SiN membrane to appear black ($\sim$500 counts). And the normalized intensity can establish the thickness of residual membrane in those holes of the array that do not fully perforate (table 1). The CCD response is not perfectly linear, but sufficiently reproducible to enable relative intensity absorbed to measure relative thicknesses of residual membranes. There is sufficient electron transmission such that differential charging does not cause instability during image capture at low magnification. For image capture at high magnification, no objective aperture is required to provide phase contrast; and drift stabilization is necessary to accommodate local charging. Fully perforated holes are imaged with 0–500 nm defocus by Bright Field TEM (figures 2(g)–(j)), however, holes with residual membranes require 1–2 $\mu$m of defocus and no objective aperture to provide extra phase contrast for image capture (figures 2(k)–(p)). Extreme defocus alters the measured diameter of the holes and is avoided during metrology, but this error is much less than the value of the asymmetry ($>$10 nm) observed.

Array processing of holes is reproducible, as long as charge/drift is not greater than the hole diameters. Figures 2(e) and 3(a) are two of ten arrays of holes identically processed. Because of the high current density of the FIB and the nonconductive nature of the membrane, localized charge builds up during processing of an individual hole/pit in spite of charge neutralization procedures. For example, figures 2(g) and (j) exhibit asymmetry due to a change in the electric field associated with the hole/beam interaction as the hole is being made. The scanning of the ion beam will help mitigate the charge/drift issue, and thus holes with the longest exposure in the smallest area fared worse. For example, holes 4–4 and 4–5 were etched the longest to an effective depth of 20 000 nm. Although these two holes were patterned to be 30 and 25 nm, respectively, the overetching caused the holes to erode to $>$50 nm; and the coupling of high aspect ratio and local charging caused them to become severely asymmetric. All small holes exhibit asymmetry; however, it can be quite reproducible between each hole array. Holes reduced to the size of the beam can exhibit asymmetry due to focusing lens astigmatism and 'hot-spots' in the beam. Mostly, however, holes of high aspect ratio have poor cylindrical shape due to charge/drift instability that then complexes the redeposition distribution within the bore. Note that varying defocus allow live TEM observation of an irregular sidewalls, but a captured TEM image is a 2D projection with all irregularities in the bore appearing as an averaged asymmetry.

*2.2.2. Erosion closure of hole and pit arrays in 400 nm thick membranes (frontside and/or backside field exposure).* Figures 3(a)–(e) provide sequential FIB images acquired after an entire array area ($\sim$90 $\mu$m$^2$) is further exposed to ion erosion at a low dose rate ($3.5 \times 10^{14}$ ions cm$^{-2}$ s$^{-1}$). Figure 3(a) is an array processed the same as that imaged in figure 2(e). Figures 3(b), (c), (d), and (e) are after eroding 10, 20, 30, and 40 nm from the entire array area. Such ion beam exposure may cause holes to close [5, 36, 43, 62], and the judicious monitoring of the hole closure enables the production of smaller holes than can be made by FIB opening a new hole. If/when atoms on a surface are given sufficient energy, then surface diffusion will mitigate excess surface energy by flattening surface topologies, and this can be enhanced by increasing the temperature of the substrate during ion beam processing [2, 5, 25, 26, 63]. Diffusing atoms will tend to fill in holes and pits. Surface temperature is modest when FIBing, and TEM samples show most materials never exceed $\sim$30 °C, as compared to 200 °C possible for traditional Ar ion milling. However, in all high energy particle physics an argument can be made for high temperature at short spatial and very short temporal scales [51].

During the formation of the array of holes, a small focused beam was used of $\sim$10 nm Gaussian width and a current of 10 pA. However, during the ion beam exposure, the beam is defocused to $>$200 nm, as well as scanned over a 10 $\mu$m wide area of the entire array using a current of 50 pA that removes $\sim$5 nm thickness per minute. In this defocused condition, a FIB acts similar to a dose from a large static ion beam. However, in all cases each ion with the same high energy individually interacts at a local position on the surface with its own localized angle of inclination and with its own individual response of redeposition due to that local surface shape. In essence, when a single pit/hole is being etched by a FIB, the centroid of the focused beam is etching at one pixel, but 'ion beam exposure' is simultaneously (within the same 100 ns of dwell) occurring at adjacent pixels due to the beam tails that spread beyond the Gaussian profile. In a traditional approach to ion erosion, each subsequent ion arrives soon enough after the previous ion that only the etching caused by each ion is considered. However, in a condition where diffusion and redeposition may be occurring, the time in between each sputtering ion is allowing for material to deposit. A possible condition is that more material might deposit during the time between the two sputtering ions impacting a specific pixel than is removed by the sputtering ions. Such a condition is possible independent of scanning FIB or big static beam, and it would be the case in an area where a hole closes.

Using the secondary contrast in the FIB images, with bright as a means of detecting fully (or almost) penetrating holes, figures 3(a) through (e) show that most small holes fully

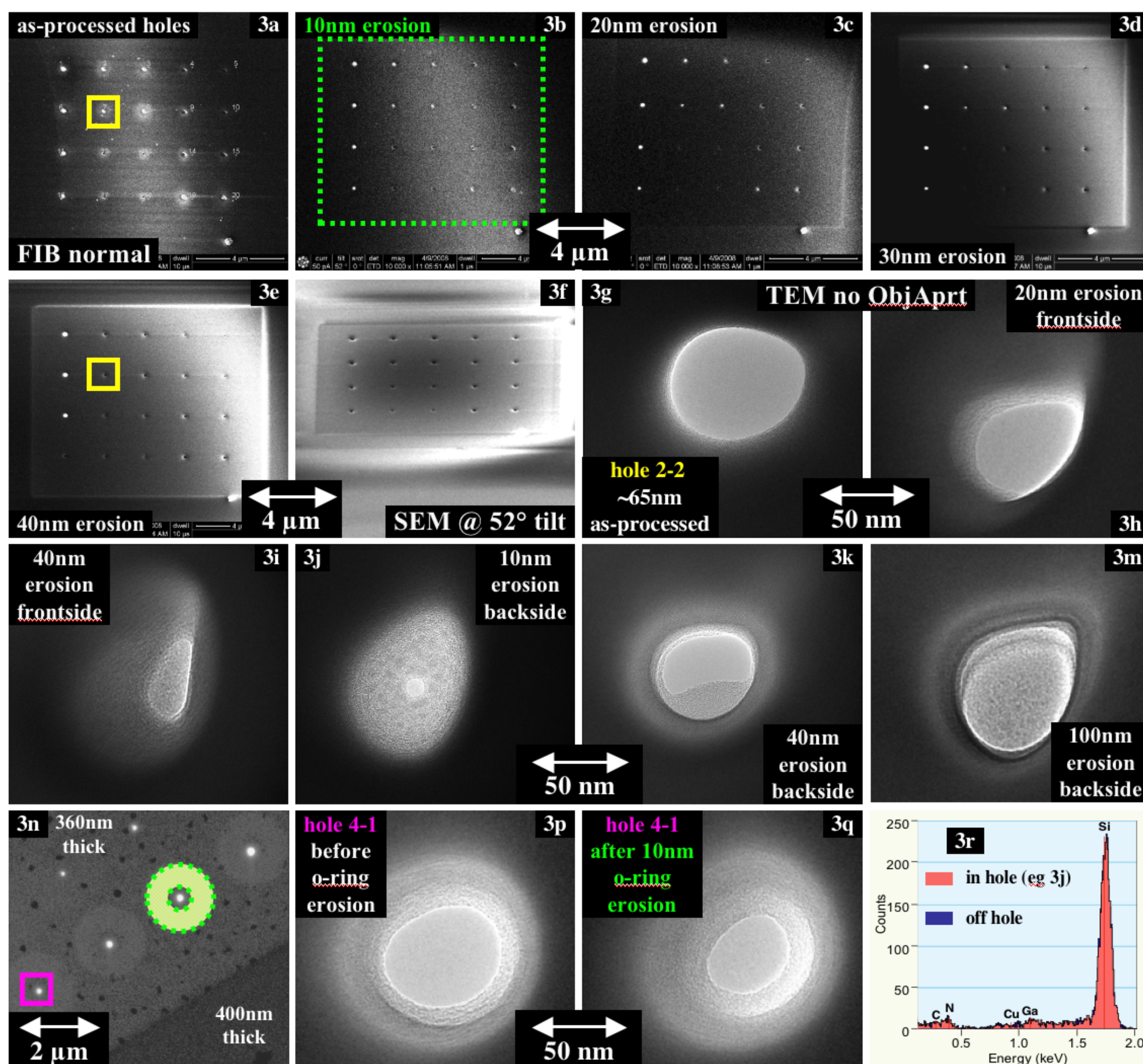


**Figure 3.** (Colour in the electronic version of the journal) ((a)–(e)) FIB images of array of holes through ∼400 nm thick SiN membrane, as-processed (a) and after erosion exposure to overall area to remove 10, 20, 30, and 40 nm. Erosion exposure causes holes to close, detected by lost transmission. Imaging contrast also shows 10 nm exposure removes charged particles noted in figure 2(e), as well as modifies the top rims of holes to reduce their contrast, too. Contrast in (e) is due to complex charging; 30 kV ions do not penetrate through the ∼400 nm thick membrane, thus no transmission contrast is detected during erosion. (f) SEM image acquired of hole array after 40 nm erosion shows the top rims of all pits erode larger, but cannot determine which have closed. ((g)–(m)) TEM images with no OA showing closure of hole 2–2 after different erosion exposure: 20 nm and 40 nm from the frontside; turned over and 10, 40, and 100 nm erosion exposure from the backside. (Frontside of these membranes is defined per figures 2(a) and (b) as the flat surface released from the Si wafer after Si etch; backside is the top growth surface of the SiN membrane, which has growth nodular roughness.) TEM images are rotated between each sample loading; however, asymmetry of hole shape is similar in each array. ((n)–(q)) low and high magnification TEM images before and after exposure to o-ring erosion (OD = 1500 nm, ID = 500 nm), causing further hole closure. (r) EDS spectra acquired on/off closure membrane in a hole (e.g. figure 3(j)). N is a weak signal for TEM-EDS, but DTSA calculations for ∼400 nm thick SiN membrane measure a Si:N::3:4 composition away from holes, and 3:1 inside the hole. Ga concentration is 0.2 to 1%, but is enriched in surfaces.

close during the ion beam exposure. Even the largest hole at position 1–1 closes from ∼150 nm diameter to ∼125 nm during 20 nm of erosion. (See table 1.) Holes of small diameter and high aspect ratio close faster, i.e. with less exposure. For example, holes 4–4 and 4–5 close faster than hole 2–2 (figure 3(d)). As-processed in the array, hole 2–2 has a 65 nm wide opening, and hole 4–4 is 75 nm wide. After 20 nm erosion exposure, hole 4–4 closes to 35 nm, whereas hole 2–2 closes only to 50 nm. Note the designed pattern hole diameters are 60 and 30 nm, respectively for holes 2–2 and

4–4. However, hole 4–4 had to be processed with excessive overetching (20 000 nm) to overcome redeposition, and its high aspect ratio continues to make it close easier than hole 2–2.

Even though the additional ion beam exposure is incurred with a beam size much larger than the holes, SEM imaging after exposure shows the top rim diameter of all holes (and pits) erode to a larger diameter (figure 3(f) compared to figure 2(d)). In addition as the rims erode larger, they also erode to a more-gentle slope. Thus the secondary emission ring contrast lessens and holes 4–2 and 4–3 become less visible in figure 3(f). Although the secondary contrast of a FIB image has the complexity of signal from holes penetrating the membrane plus signal from top surface emission, the FIB images confirm that the rims erode to a more-gentle slope. In the as-processed hole array, the rims appear bright in the FIB image (figures 3(a) and (e)) because the sharper angles cause more brightness in secondary emission. With only 10 nm of exposure, however, figure 3(b) shows less brightness at the rim of the holes indicating the slope has been dramatically flattened. Another interesting effect caused by exposing the whole area is the immediate removal of all the excess particles that had accumulated during the complex charge distribution caused during the discrete array processing. This removal of charge particles occurs with minimal exposure, only 10 nm in figure 3(b).

Figures 3(g)–(m) are TEM images depicting the hole at position 2–2 of the arrays after various erosion exposures. All arrays exhibited hole 2–2 as fully penetrated with a diameter of 65 nm $\pm$ 10 nm prior to the additional ion exposure. FIB imaging determines hole 2–2 becomes fully closed somewhere between 30 and 40 nm erosion exposure (figures 3(d) and (e)). TEM after 20 nm erosion (figure 3(h)) shows the hole is closed to $\sim$50 nm; and after 40 nm erosion (figure 3(i)) the hole is completely closed. Also asymmetry of the hole worsens to more than $\pm$20 nm as it closes in figures 3(h) and (i). (A model of atom motion by pure surface diffusion might argue for a reduction in asymmetry during hole closure. Also diffusion of more atoms would be required to close a hole of high aspect ratio, i.e. to fill a thicker membrane. Thus with minimal thermal assistance, surface diffusion may close a hole in a thinner membrane easier.) Subtle tilts during TEM imaging confirmed holes could have a $\pm 1^\circ$ variation of inclination, and the asymmetric tilt could change along the bore of the holes, thereby affecting shape of hole closure. For the holes in figures 3(j)–(m), the membrane was turned over and the array exposed to backside erosion for 20 nm, 40 nm and 100 nm, respectively. (More discussion of backside erosion is presented for thinner membranes in figure 4.) Although trends for the several hundred holes all showed holes closing with ion exposure, the closing rate appears stochastic and thus the hole after 20 nm exposure can sometimes be smaller than the hole after 40 nm exposure (figures 3(j) versus (k)). End-point detection needs to be spatially discriminating to individually monitor holes.

Through-focus TEM imaging on the hole after 100 nm exposure (figure 3(m)) determines the bore of the hole is not smooth, and holes starting with a smaller diameter (therefore higher aspect ratio) exhibited more severe sidewall irregularity. Since these bore irregularities worsen during this erosion exposure process even with its more stable charge distribution, then much of the worsening asymmetry appears due to stochastic effects such as redeposition. Conversely, purely diffusional processes would be expected to smoothen irregularities within the bore. Using TEM intensity as a measure of residual membrane thickness (table 1), 100 nm of exposure caused this closing hole to develop a membrane $\sim$100 nm thick (figure 3(m)). However, where within the $\sim$400 nm long bore of the aperture this membrane resides is not well controlled.

Both backside and frontside erosion cause hole closure in thick membranes. Backside exposure may provide a more-gentle closing process than can frontside exposure, as shown in figures 3(k) versus(i), respectively. 40 nm exposure to the backside closed the hole by forming a thin coating $<$10 nm thick and keeping much of the bore of the hole still open (figure 3(k)). Conversely, frontside exposure of 40 nm closed the hole with a coating $>$50 nm thick. Hole closure from frontside erosion also produced worse asymmetry, which is exacerbated by alignment issues of sample tilt and flatness. A pre-hole at an angle (even $<1^\circ$) encourages asymmetric redeposition down its bore, and this effect is lessened by backside erosion. Another difference between frontside and backside exposure is that the latter appeared to cause some holes to open a little ($<$10 nm) prior to closing. This initial opening was only observed in the largest diameter ($>$100 nm) holes. The differences between frontside and backside exposure may be arguments for diffusion control of the closing process, because redeposition should be lessened for a flatter backside. On the other hand, if dense (thick) closure of holes is desirable, then frontside exposure may allow extra redeposition down the sloping sidewalls to close the hole more fully with less exposure.

*2.2.3. Near-field erosion closure.* To further test the extent of redeposition, individual holes are exposed to near-field erosion. Redeposition remains an inexact science in all ion beam processing, not only for hole closure. What is the redeposition material? Where is the material redepositing? How far does redeposition travel? Quantifying these answers are necessary to establishing how redeposition plays a role in ion beam physics such as hole closure. 'When an ion beam is sputter etching a trench, can redeposition get into the previously processed trench 1 $\mu$m away,' and cause leakage current or potentially short the previously processed device? [64]. 'When ion beam processing an aperture, can backsputter redeposition from somewhere else lead to hole closure of a different material on the backside?' [43, 65, 66]. Figures 3(n)–(q) present results for 'o-ring' erosion exposure for holes through the thick SiN membrane; however images in figures 4(s)–(v) of holes through the thin SiN membrane help elucidate the experimental process. FIB computer control enables the erosion of o-rings (presented as an overlay onto the TEM image of figure 3(n)) of 1500 nm outer diameter, 500 nm inner diameter and depth of 10 nm using a 10 pA beam of $\sim$10 nm spot size. From earlier results, the beam tails can cause slow erosion 100 nm away from a 10 nm focused spot, and even at the center of the o-ring

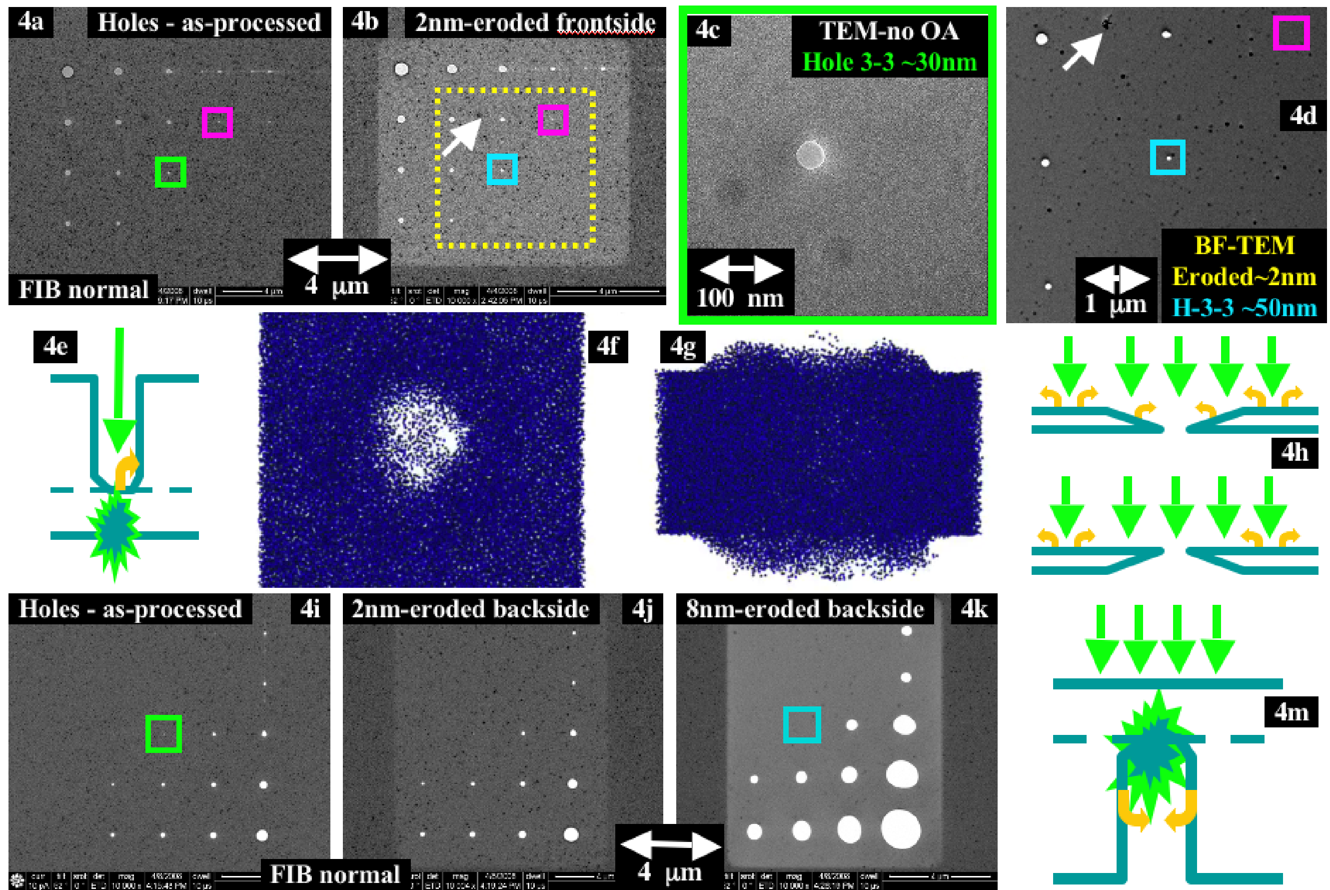


**Figure 4.** ((a), (b)) FIB images of array of holes through a ∼20 nm SiN membrane as-processed and after 2 nm erosion exposure on frontside. Imaging contrast includes signal from FIB transmission, making brighter the area that has been eroded thinner in (b). ALL holes that fully penetrated the membrane eroded open with exposure. Pits, which had not fully penetrated, closed (red box). ((c)–(d)) TEM shows hole 3–3 eroded open from ∼30 to 50 nm with 2 nm exposure, but pit 2–4 has completely filled and is no longer visible (red box). (e) Schematic akin to figure 1(c) applied to thin membrane shows hole explosively forms upward from the bottomside due to high energy ions penetration. This leads to a hole diameter with a minimum size dictated by ion implantation cascade diameter (∼20–30 nm for 30 keV ions). ((f), (g)) Snapshot images, topview and sideview, from models of ion erosion through membrane. (See [52, 70] for more details.) To reduce computer calculations, energy of ions is 1500 eV and film thickness 6 nm. Each spot represents an atom, as frozen in place after several picoseconds of relaxation after ion impact. Other models show both top-down and bottom-up pits meet to produce aperture hole. Redeposition is present on both topside and bottomside surfaces after just a few ion impacts and before hole fully opens. (h) All FIB-processed holes (and pits) will have sloped sidewalls, worsened by beam tails and by aspect ratio of hole. Thus frontside and backside erosion exposure will have different influence on further redeposition that may close holes. ((i)–(k)) FIB images of as-processed and after backside erosion exposure of 2 and 4 nm. All open holes erode bigger, and 'faster' than by frontside exposure. However, non-fully-penetrating pits can close faster, too. Dark spots in transmission images represent regions of membrane that are thicker due to nodular film growth; nodular roughness is smoothened by backside erosion, (e.g. (k)). (m) Schematic how bottomside redeposition explosively fills a non-penetrating pit faster than it can explosively sputter open upwards. ((n)–(q)) TEM images of a non-penetrating pit before and after backside exposure. BF-TEM and HR-TEM show precipitates of Ga have formed encapsulated in the closed pit. (r) Rastering the FIB beam, even over dimensions smaller than the beam profile, enable overlapping redeposition to close bottomside pit before it can explosively open upwards, thereby slowing hole penetration and enabling a smaller diameter hole to form. ((s)–(v)) FIB, SEM and TEM images of o-ring erosion exposure, which causes holes to further open for thin membrane. O-ring ID is ∼500 nm, but beam tails make ID < 400 nm. The thinner membrane makes the o-rings visible due to enhanced transmission in all three microscopies.

some effect of beam tails may remain. Figures 3(p) and (q) are of hole 4–1 in the array, exhibiting diameters of ∼60 nm before and ∼40 nm after o-ring exposure respectively. In this case, hole 4–1 had been partially closed by 40 nm backside exposure prior to the o-ring exposure of 10 nm, thus the diameter of ∼60 nm in figure 3(p) is already closed from the as-processed ∼100 nm diameter of figure 2(h). More discussions of the o-ring results are presented for figure 4(s).

*2.2.4. Chemical analysis of closure material.* Figure 3(r) presents two overlaying energy dispersive x-ray spectra (EDS) acquired of material in a closing hole (e.g. figure 3(j)) and of the surrounding membrane, red and blue respectively. Two major flaws with chemical analysis are geometry and dirt. The take-off angle of the EDS detector in a TEM coupled with the high aspect ratio of holes in this 400 nm thick membrane means that the majority of the signal detected is from the membrane surrounding the hole. Secondly,

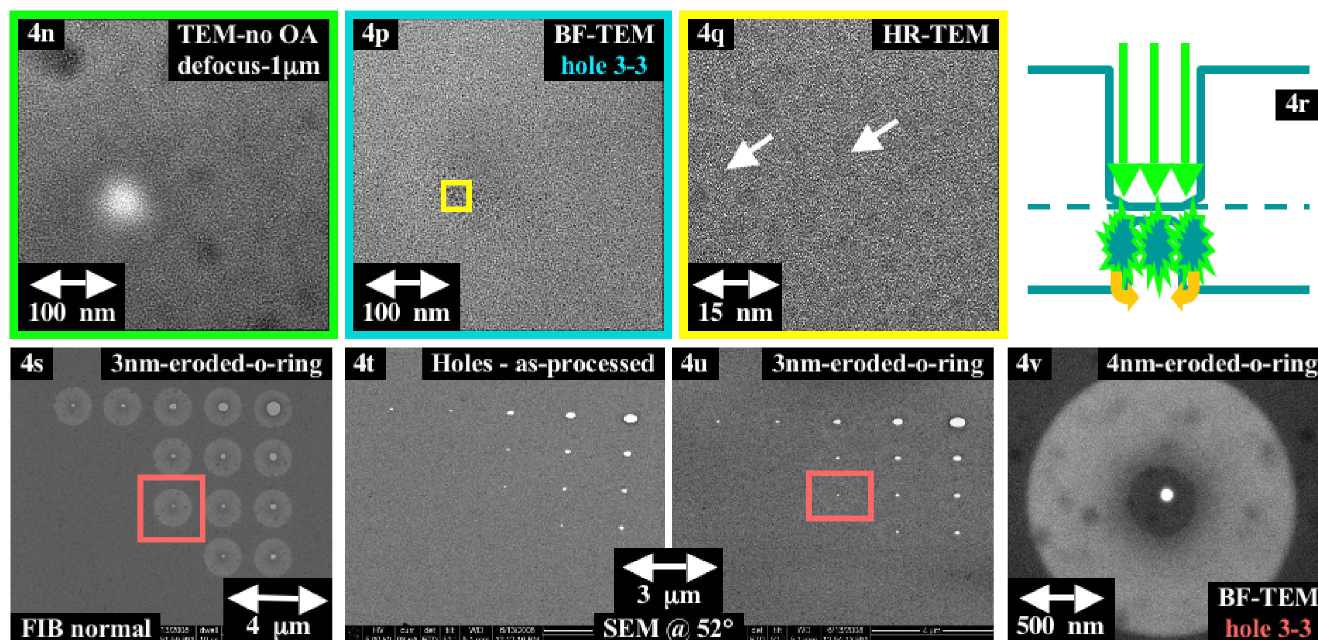


**Figure 4.** (Continued.)

the high current density focused to analyze the membrane causes local adsorbed carbon contamination to build up [67]. Diffusion of carbon induced by the electron beam is often judiciously controlled to process hole closure [36]. STEM is used in this case with constant scanning to prevent the C signal from growing; however, holes eventually closed during STEM analysis, and EDS detected corresponding carbon increases. For these hole array experiments, the SiN membranes were cleaned by plasma cleaning prior to initial FIB processing of the holes, using methods typical for cleaning TEM samples [68]. However, plasma cleaning was avoided between repeated imaging/processing transfers to prevent possible erosion artifacts of the holes themselves. Thus some holes may have been exposed to environmental hydrocarbon contamination and this C source enabled TEM-induced closure of holes in the thick membranes. FIB can cause growth by CVD so when sufficient carbon is available and for low dose rate conditions to minimize ion etching, then carbon closure of holes is possible in the FIB, too. However, the lack of carbon in the EDS in figure 3(r) indicates holes can be closed by FIB without carbon.

EDS in high-voltage TEM is also poorly sensitive to low-Z elements such as nitrogen, and this is relatively worsened in thick membranes. The spectrum from the thick membrane exhibits a weak N signal compared to Si; however, DTSA[1] computations establish this is the correct 3:4 ratio for Si:N in a 400 nm thick membrane and the take-off geometry and window configuration for this Oxford EDS detector. Thus using the membrane as a standard, the composition of the hole closure material is established as Si-rich. Although sputter theory alone indicates steady state erosion removes Si and N together, redeposition and/or diffusion of Si is much preferred over N. Therefore, the closure material in the hole being more than doubly Si-rich is not unexpected. Ga is detected in both spectra, as the surrounding membrane had been eroded for 10 nm. The Ga concentrations (0.2 and 1.2 at.%, on the membrane and in the hole, respectively) seem modest, but actually this represents significant Ga in the top few atom layers. Ga can also coalesce and precipitate (see figure 4(q)).

*2.2.5. Array processing of pits and holes through 20 nm thin membranes.* Figure 4 presents one of a dozen hole arrays processed through a thinner (∼20 nm) silicon nitride membrane. The same 10 pA (∼10 nm diameter) FIB beam was used as for the thick membrane; however, the durations of etching (effective depths) were reduced. Hole diameters were patterned as 100, 50, 20, 10, and 3 nm for the 5 columns, and depths of 5000, 500, 100 and 30 nm for the rows. Again all effective depths should be greater than the membrane thickness of 20 nm; however, reduced yield for high aspect ratio again precluded penetration for the smallest holes. When the hole is a sufficient diameter such that aspect ratio is $\ll 1$, then 30 nm of etching easily perforated the membrane (e.g. hole 4–1). However, for high aspect holes, even 500 nm of etching could not perforate the membrane (e.g. hole 2–5). On the other hand, even when a hole is patterned smaller than the beam diameter (e.g. the 3 nm holes in column 5), excessive overetching can eventually erode a hole to a large enough diameter that it eventually perforates (e.g. hole 1–5). Unfortunately, it is again observed that this excessive overetching eroded the '3 nm' hole to >50 nm. The overetching caused by beam tails always make the diameter of the top rim larger (upwards of 100 nm), however, its gentle slope may preclude observation by SEM.

The FIB imaging of the thin silicon nitride membranes differs from imaging the thick membrane. Sufficient ions pass through the entire thickness of the membrane that FIB imaging can be treated akin to TEM. Brightness primarily represents penetration, and secondary emission due to topology at the

[1] DTSA is a NIST program available for EDS spectra quantification in electron microscopes.

rim of holes comprises a minimal component of the image. Secondary electrons are emitted from all top surfaces, thus end-point detection must be geometrically controlled to make transmission the major portion of the signal. Furthermore, erosion exposure to remove only 1–4 nm of the membrane thickness becomes detectable as a brighter background (e.g. figures 4(b), (j), (k)). Also the FIB penetration through a thin membrane precludes as much charge build-up, thus no flood of electrons was needed during the hole array processing of thin membranes. All FIB imaging is destructive, but these medium magnification FIB images can be acquired with $<1$ ML of material removal. Thus FIB imaging can monitor holes that erode bigger due to only 1–2 nm removal from the surroundings. FIB transmission images can detect 3D shape of holes in thin membranes, however the FIB damages sufficiently as it observes at high magnification and is too destructive for accurate metrology of the shape of the hole sidewalls.

*2.2.6. Erosion opening of hole arrays in 20 nm thin membranes.* All perforated holes through the thin membrane eroded to grow larger during the subsequent ion beam exposure. This represents $>100$ holes in $>10$ arrays with only one anomalous hole at position 3–1 closing in one array due to a defect (possibly a particle or nodule). These opening holes are in complete disagreement to holes through the thicker membrane, which all proceeded to close. The erosion exposure upon the processed holes used the same defocused 200 nm beam, but with a lower current (10 pA and dose rate of $7 \times 10^{13}$ ions $cm^{-2}$ $s^{-1}$) such that erosion removal was $\sim$1 nm $min^{-1}$ over the field of the array. (A higher beam current erodes holes open too fast for study.) Figure 4(b) depicts holes enlarging after 2 nm of erosion exposure. Figures 4(c) and (d) are TEM images before and after 2 nm erosion, respectively. Hole 3–3 is fully perforated and $\sim$30 nm in diameter as-processed and then enlarges to $\sim$50 nm diameter after 2 nm of erosion exposure. Because the membrane is sufficiently thin for electron penetration, the higher magnification TEM images of the thin membrane can be captured at (near) traditional Scherzer defocus to provide precise metrology. The lower magnification images are still best acquired with BF imaging conditions. Both FIB and TEM images depict 'black spots' (e.g. arrow in figures 4(b) and (d)) which are regions of membrane that are thicker. Thick and thin silicon nitride membranes exhibit nodular growth morphologies on the top surface. Although the nodules manifest as larger bumps for the thicker membrane (even resolved by SEM), they represent a greater increase in relative thickness for the thin membranes and thus are more visible as dark regions in transmission images of thin membranes. Because of the complex contrast mechanisms in the FIB image, detection of non-fully perforated holes can be questionable; however, previous results have shown the TEM to be quantitatively sensitive to holes and pits that do not perforate [59]. Reliable measure of the 3D shapes of these holes/pits require TEM imaging parameters and cleanliness to be controlled to preclude TEM-activated closure/opening of small holes [67]. Attempts to cross section small holes for analysis can cause damage to the hole during preparation, therefore through-foil TEM can provide more robust metrology. Through-foil TEM is also sensitive to thickness changes of only 1–2 nm when comparing the erosion exposure region to the unexposed membrane (e.g. figure 4(v)). Figure 4(d) shows no residual partial holes nor pits remain visible at positions 3–4, 4–3, and 4–4 after the 2 nm of erosion exposure.

Hole closure has been developed as a process primarily because FIB etching cannot make a small enough hole [5, 36, 40, 43]. The nature of hole drilling, especially coupled with redeposition within a hole, should manifest as a hole just beginning to perforate at the center. I.e. the bottom of a crater is not atomically flat and typically erodes deeper at the middle. (During the scanning process of the FIB, there are several computer-controlled issues that undesirably make dwell time at each pixel of the scan not equal [4, 59, 69]. And this can artificially lead to more extensive etching at the edges of some patterns.) A patterned hole can be eroded bigger than the pattern by extensive overetching; or large patterned holes can be perforated as smaller than the pattern by underetching. However, in all of these hole arrays, the as-processed holes are never smaller than 25 nm (e.g. figure 4(c)); and only by hole closure methods in the thicker membranes can a smaller aperture be achieved (e.g. figure 3(j)). Thus an interesting question is 'Why does the FIB never make a hole that is smaller than $\sim$25–30 nm in diameter?'

Figure 4(e) applies the schematic of FIBing a pit (figure 1(c)) to a membrane, and considers that the incoming 30 keV ions have a natural implantation depth of tens of nanometers [3, 31, 32]. When the pit has reached some critical depth, it becomes statistically more likely that the ion will impart its energy through the residual membrane and to the bottomside of the membrane. And in this geometric condition the sputtering yield out the bottomside of the membrane is dramatically higher than the yield upwards out of the hole. This effect is further enhanced as a consequence of redeposition effectively dropping the yield up out of the hole from the top. Once this bottomside etching effect starts, it quickly cascades upwards, as the membrane gets sequentially thinner faster. The resolution of the top-down sputtering is modeled as confined to within $\sim$1 nm of the individual incident ion [32, 19]. However, the bottomside sputtering has a resolution dictated by the implantation cascade which has been modeled as tens of nanometers wide and expands with increasing energy of the incident ion [4, 31, 32]. Thus the bottomside sputter pit opens to tens of nanometers for a 30 keV FIB, and this determines the minimum size of the hole that explosively forms. Note that although a top-down pattern $<10$ nm diameter may be imposed, erosion by FIB beam tails causes such holes to have sloping sidewalls and the top rim can extend to $>100$ nm depending on membrane thickness (figures 2(d) or 3(f)). But the bottom of the hole will always break through via bottomside sputtering and explosively open to 20–30 nm. For very thin membranes (and also for cutting nanotubes or nanowires with a FIB), the high energy of the incident ions can cause the hole to even start etching at the bottomside first [52, 70].

*2.2.7. Bottomside sputtering and redeposition.* Figures 4(f) and (g) are snapshot views, top-down and sideview, respectively, from Zepada-Ruiz' modeling of the ion sputter etching through an amorphous membrane [70]. In order to reduce the calculations in this case, the energy of the incident ion is reduced to 1.5 keV and the membrane thickness is 6 nm. The snapshots show the conditions after the 25th ion has impacted. More details of how the modeling is performed are presented elsewhere [52, 70], with a primary consideration being that after each impact there is some recovery period of picoseconds to allow atoms to try to get back to their positions before the next ion can be impacted. Even in the highest current densities of the most focused ion beams, the time between contiguous impacts is on order of nanoseconds. A 10 pA ion beam current focused to a 10 nm probe size means ~16 ps between ion hits, but 125 ns between ions hitting the same exact 1 Angstrom spot. Thus for sputter theory resolution of 1 nm, the time between impact events can be long (>100 ns); but for the 10–30 nm resolution of implantation cascade theory [3, 51], there may be temporal overlap between ion impact events. All modeled relaxation events are typically frozen within a few picoseconds so that cross talk between successive incident ions can be neglected in modeling. (Increasing the duration of relaxation, but without cross talk, leads to more ions required to perforate the hole.)

The sputtering yield for most materials is on order 1–10, however, several models show an impacting 30 keV Ga ion will cause thousands of atoms to become displaced as the energy is absorbed [3, 4, 10, 31, 54]. Many recover to original atomic sites in the (crystalline) solid, but not necessarily each individual atom to its original site. The Zepada-Ruiz model [70] also shows many atoms can 'redeposit' on the surface around the rim of the forming hole, although with time and mobility such atoms can migrate back into the hole to reduce surface energy. For an experimental focused ion beam, the beam tails extend well past this region of redeposition, and thus most of the stable redeposited material outside the pit is removed faster than it accumulates. Of more interest are the redeposited atoms on the bottomside of the membrane. For high energy/low thickness conditions of membranes, these bottomside sputtered atoms can start redepositing with the first ion impact, well before the hole perforates. Furthermore, these bottomside atoms can geometrically show a greater lateral dispersion of the redeposited material, which experimentally is not removed by beam tails.

Although these snapshots (figures 4(f) and (g)) can only provide a limited view, watching a movie of the Zepada-Ruiz model [52] shows the hole does not form solely at the single atom site where the ion beam impacts [70]. Rather the hole 'explosively' forms directly to a diameter of several nanometers; and the sideview shows this explosion results in many more atoms expelling from the bottomside. In this model each successive ion impacts at the same central pixel; however additional models have scanned the FIB beam to make a more random positioning as would occur even if a Gaussian FIB probe possibly becomes focused to subnanometer. (He ion microscopes are approaching 0.1 nm resolution, but do not provide ion sputter erosion [71].) When the incoming ions are rastered over an area (even <1 nm diameter), the explosion process becomes more stochastic; the hole can start to open, but then close, and it takes many more ions before it fully opens. However, the models also indicate that such rastering can lead to an incipient (stable) hole that is smaller in diameter than a hole formed without rastering. This is often experimentally observed [59], that rastering a 10 nm FIB over a 5 nm area can actually lead to a more reproducible small hole, albeit always >20 nm as a minimum. (See discussion for figure 4(r).) Once the hole is open, all subsequent incident ions go through the hole and no energy is imparted to the membrane. And since the modeled ions have excellent precision, limited angle of convergence, no beam tails, and membranes with low aspect ratio holes; then once a critical size hole forms it remains stable. Sputtering stops. Beam tails in a real FIB extend >100 nm and continue to erode the hole bigger (as well as enabling redeposition events) during overetching processes. However, the diameter of these stable model holes do not correspond to a calculated sputter resolution of ~1 nm but rather to an implant-modeled resolution of several nanometers for a 1000 eV ion and of 20–30 nm for a 30 keV Ga ion. Sputter etching out the bottomside dictates the minimal hole size.

Figure 4(h) schematically considers cross-sectional views of two options for erosion exposure upon the pre-processed holes. Erosion can be conducted from the frontside, or the membrane can be turned over and exposed from the backside. All as-processed holes through all membrane thicknesses will naturally erode their top rims to a greater diameter than inside the bores of the holes, creating sidewall slope. Note this is for experimental holes which in practice are >30 nm in diameter. Furthermore, the hole may always have an hourglass shape due to bottomside explosion. However for thicker membranes and higher aspect ratios, the erosion at the top will always cause the top rim to be larger than the bottomside rim. Thus, for the pre-processed condition in figure 4(h) the bottomside explosion is temporarily ignored and the sidewall slope exaggerated.

During the subsequent erosion exposure, several nanometers of material are being removed from the surface. However, at the local site of each incident ion, there are local perturbations in the surface; thus some (differing) degree of redeposition is occurring everywhere. Since the bore of the hole has a slope, the amount of redeposition inside the hole due to the slope should be greater. Frontside and backside erosions upon these holes with sloped sidewalls will manifest a difference in redeposition, with the expectation that redeposition should be less for the backside experiments. Conversely, if the majority of atom motion occurs due to surface diffusion, then the tendency to close holes should be the same for both frontside and backside exposure. The energy enabling diffusion will be less imparted on a tilted surface, thus diffusion-controlled hole closure is actually slightly more favorable via backside exposure. Even if the membrane is so thin that most ions impart their energy to mobilize atoms on the opposite side, surface diffusion would act the same way to try to mitigate surface energy by closing holes. However, for such thin membranes backside etching is not expected to encourage more redeposition within the hole, especially at the thinnest rim of the hole in schematic of figure 4(h).

The experimental results for backside erosion exposure of the array of holes through the thin membrane are presented in FIB images of figures 4(i), (j), and (k), respectively as-processed, exposed to 2 nm of erosion, and 8 nm erosion. As earlier noted, all perforated holes eroded to become larger in the thin membranes independent of frontside or backside exposure. Also comparing figures 4(j) and (b), it appears that backside etching erodes holes larger with less exposure. This is consistent with the comparison of backside and frontside erosion upon the array of holes through the thick membrane. Even though the holes close in the thick membranes, figures 3(i) and (k) show closure requires more exposure on the backside. Redeposition within a hole is more pronounced when coming from the frontside and especially when the hole has a high aspect ratio and the corresponding sloping rims. Since the backside is flatter, redeposition can be minimized. However, for holes of high aspect ratio even if backside etching erodes open the backside rim, eventually redeposition within the bore of the hole will cause it to close (figure 3). And a high aspect hole can be closed faster via frontside exposure due to redeposition down the sloped sidewalls.

*2.2.8. Backside erosion for bottomside redeposition on the frontside to encapsulate dots.* When the schematic of backside etching in figure 4(h) is applied to a not-quite-perforating pit, it may be expected that such holes should open. Not only does pit 3–3 refuse to open to become a hole, but also it becomes invisible during the backside erosion from figures 4(i) to (k). This pit, which had been fabricated >80% of the way through the membrane, refused to open even though nearly half of the membrane has been removed from the backside, as indicated by the increasing brightness of the background with 8 nm FIB erosion. The backside erosion also removes the dark speckle of the nodules, and this is common for a FIB scanning normal to the surface to smoothen a nodular growth surface [45, 19, 39]. Both array-hole processing and 'frontside' exposure are performed on the non-growth side of the SiN membrane, which is (near) atomically flat after chemical-etch-removal of Si substrate. Thus nodular smoothening can only occur during the 'backside' erosion exposure in these experiments. Without the extra contrast from surface nodules, the FIB transmission intensity can more certainly establish non-perforated pits disappear with backside exposure. Figure 4(m) presents a schematic of ion exposure to the backside on a non-perforating pit. The energetic ions that transmit through the residual membrane cause bottomside etching along the sidewalls of the pit, which in turn causes redeposition within the bore of the pit. Since implantation has a lateral spread of ~30 nm, the backside scanning ±30 nm either side of the pit all causes bottomside redeposition within the pit. Furthermore, the bottomside sputtering effect follows implantation theory and involves hundreds of atoms moving, all of which relax and redeposit so as to best fill the pit. All this redeposition easily compensates for the traditional sputter etching that is making the entire membrane thinner, but which follows topside sputter theory that yields a few atoms removed per ion. An upside-down pit, being filled by bottomside redeposition, never meets up with the topside erosion to provide perforation.

Figures 4(n) and (p) are TEM images of this pit 3–3 before and after 8 nm of backside erosion exposure. Not only is the non-perforated pit becoming less transparent by filling in from redeposition on the opposite side, but also there are small darker features within the location where the pit had been. figure 4(q) is a high resolution TEM image with lattice fringes corresponding to Ga. As the Ga implanting from the backside caused redeposition to fill the pit, the redeposition also traps those Ga ions that implant that deep. More importantly, the original pit formation by FIB causes Ga along the sidewalls and bottom. These both provide a sufficiently high local concentration of Ga that creates Ga precipitates, which are then completely encased by the surrounding redepositing matrix. Other non-volatile ion species could produce similarly encased nanometer-scale precipitates (dots).

Hole 3–3 is the borderline hole of the array of holes in these thin membranes. Sometimes it perforated when the arrays were processed (e.g. figure 4(c)), and sometimes not (figure 4(n)). When a hole was open through the thin membrane, both frontside and backside erosion exposure caused it to open further. When a hole did not fully perforate, the erosion exposure caused the pit to fill in and completely disappear in both FIB and TEM imaging. Only in one case did a non-perforating hole 3–3 break through via backside etching, and once it did it continued to erode larger with more exposure.

The schematic of figure 4(r) can consider several geometric options, including both frontside and backside hole formation issues. Hole formation by FIB in most practical membranes will start a pit from the top. Also all ion beam processing, even with the most focused beam, cannot have each sequential ion impinge at the exact same Angstrom. Thus the scanned or rastered beam in figure 4(r) is a more practical description of sequential impacts, except computer scanning can provide more control than does the randomness inside a static beam. Once the residual membrane is sufficiently thin, bottomside sputtering opens a bottom-up pit and subsequent processing is the meeting of these two (top-down and bottom-up) pits. This condition similarly exists if a pre-pit had been intentionally processed followed by backside erosion. At this juncture presented in figure 4(r), each impinging ion is less likely to produce sputter yield upwards and more likely to produce bottomside sputter. Yield in the top-down pit is being reduced by redeposition; however, the implanting rastered ions also produce redeposition in the bottom-up pit. This rastered bottomside redeposition can fill the bottom-up pit nearly as fast as it bottomside sputters open. (When the pre-pit in the backside experiment has a high aspect ratio, the bottomside redeposition increases to dominate and fully fill the bottom-up pit.) This reduces the explosive opening process, enabling a smaller hole to stably form. Both modeling [70] and experiment show a rastered FIB beam can form a smaller hole (albeit still >20 nm for a 30 kV Ga ion), more reproducibly than can a stationary focused ion beam.

*2.2.9. Near-field erosion opening.* The near-field erosion experiments for the thin SiN membrane are presented in

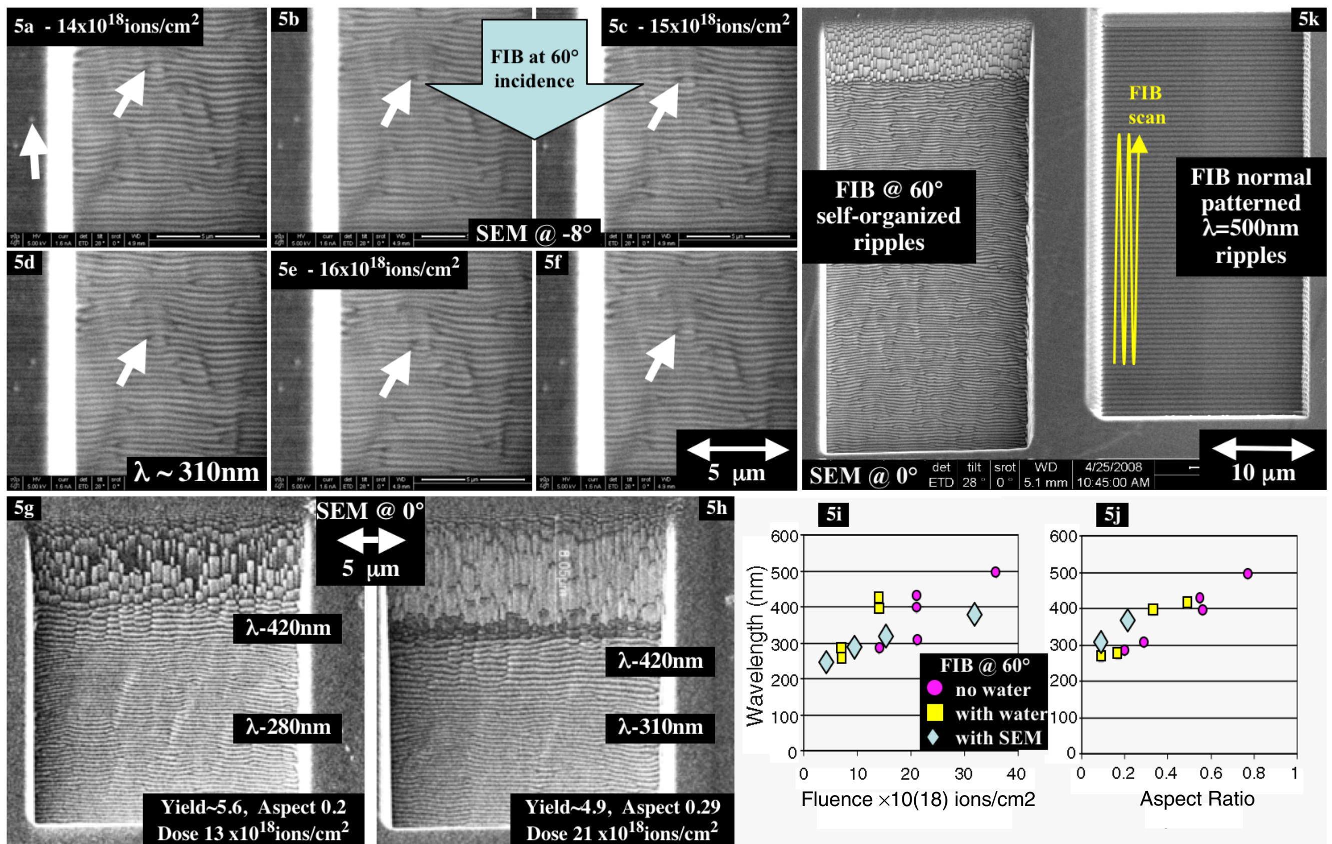


**Figure 5.** ((a)–(f)) Snapshots from SEM *in situ* movie (available at stacks.iop.org/JPhysCM/21/224013) acquired of self-organizing topologies during ion erosion of single crystal diamond. FIB inclination is 60° from the north; SEM view is 8° from the north. SEM current is increased to 1.6 nA (5 kV) and scanned out-of-sync with FIB raster to insure secondary detection matches SEM [34, 50]. Arrow at side denotes defect to left of crater used for relocating sample drift over 1 h. Arrows in middle denotes an extrinsic line fault, which jumps twice ahead of ripple motion. Edges erode faster; thus ends of line defects erode faster, and portions of ripple defects inclined to beam erode faster. Energetic considerations (surface and line-tension) predict defects should disappear, (and the density of defects does decrease as ripples grow). However, the greater redeposition downstream of an eroding defect leads to its faster motion downstream [34]. Motion of these defects thus supports the requirement of redeposition for all ripple motion and growth. ((g), (h)) SEM *ex situ* images of FIB erosion pits on diamond. Ripples form at the crater bottom perpendicular to the 60° angle of ion inclination; however, the leading sidewall (∼90°) develops 2D steps [39, 33]. ((i), (j)) Ripple wavelengths correlate better with aspect ratio of pit than with dose, although wavelength near boundaries are larger ((g), (h)). Chemical-enhanced ion etching (added water vapor for diamond) causes ripple wavelength to grow while increasing yield; but the extra energy due to SEM movie causes ripples to grow while depressing yield. In all cases ripples grow due to increasing redeposition. (k) FIB computer control can pattern ripples (right, with FIB normal), as well as self-organize them (left, with FIB inclined). Note the scan pattern was deliberately vertical to show modulations can all be due to pattern control or inclination, respectively, and not due to scanning parameters.

figures 4(s)–(v). In this case, the inner diameter of the o-rings ranged from 400 to 800 nm and was tailored to account for the diameter of the as-processed or eroded-open holes. Also the extent of etching was reduced to 1–4 nm removal, using a 10 pA (∼10 nm) beam. Figure 4(s) is a FIB image after o-ring processing, whereby the FIB brightness is enhanced in the regions of the membrane made 3 nm thinner by the o-ring erosion. (O-ring erosion was attempted on a non-perforated hole, but without any positive effects. Thus the array of o-rings is expeditiously processed only where holes are known to be fully perforating.) O-ring processing was applied to as-processed holes, as well as arrays previously eroded larger by exposure; and the hole presented in figure 4(v) had been exposed to 4 nm of backside erosion before applying 4 nm o-ring erosion. O-ring exposure was applied to the backside in order to avoid effects of original beam-tail erosion surrounding the as-processed holes. With optimized end-point detection, the SEM images of figures 4(t) and (u) measured the holes diameters before and after o-ring processing, respectively. All holes through the thin membrane opened further with o-ring exposure, both those as-processed and those also exposed to large area erosion. FIB imaging can detect the enlarging holes, however, SEM imaging before and after FIB imaging assured that no further hole opening occurred during quick FIB image acquisition.

Figure 4(v) presents a TEM image of o-ring erosion exposed to hole 3–3 (which had been previously opened from 30 to 50 nm by 4 nm of backside erosion exposure). The inner diameter (400 nm) is big enough to preclude any bottomside redeposition effects, and the membrane inside the o-ring retains its thickness. However, the o-ring exposure caused the hole to open further to ∼60 nm. Neither diffusion nor redeposition acted to try to close the hole. But apparently beam tails, greatly reduced at >200 nm, still can erode a hole open. Beam tails

are a concern in all processing, but at some distance they are measured to be safe to remove less than 1 ML by sputtering, even for processing schemes requiring hours. However, the thin edge of a pre-existing hole will be sputter etching from the bottom, with a much greater yield than the surrounding thicker membrane. Also with modest aspect ratios and flat bottomside geometries, bottomside redeposition is minimized. Conversely, any erosion caused by beam tails on a top surface is being mitigated by local redeposition. Thus in a condition which should be insufficient to enable one complete monolayer of sputter etching of the topside of the membrane, (e.g. FIB imaging condition or during o-ring beam-tail exposure) the hole in figure 4(v) can erode open due to enhanced bottomside sputtering.

### *2.3. Self-organized ripples, deposition during erosion, and erosion during deposition*

As an example of ion-induced self-organized modulations, figure 5 presents SEM micrographs acquired of the bottom of FIB-eroded craters on diamond. Earlier reports of ion beam erosion of diamond have recorded differing regimes of roughness (smooth, 1D ripples, and 2D steps) depending on angle of inclination and extent of etching [37, 39]. The ion beam inclination during the formation of these craters is 60°, however, note the tops of figures 5(g) and (h) also include the leading sidewall of the crater, which exhibits steps because it has developed at a different angle to the incident beam, closer to 90° [37, 39]. The wavelengths and orientations of ion-beam-induced surface modulations (ripples) depend on energy of incident ions, angle of incidence, fluence, species of incident ion and surface structure, as well as other controllable parameters such as temperature and chemical environment, and less understood factors such as redeposition [1, 12, 13, 19, 25, 26, 28, 39, 46, 49, 57, 73–75, 72, 76]. Although ion beam current is held constant, it is noted that yield may not remain constant during FIB processing, and changing yields may also alter topologies of modulations [1, 5, 23, 25, 37]. A saturation of ripple wavelength of ~220 nm on diamond has been reported by Datta *et al* [72] using a 50 keV ion beam at 60° incidence (and a smaller saturation wavelength for lower energy); however, growing ripples to larger wavelengths has also been observed as well as a dependence on boundary conditions [37].

Figures 5(a) through (f) are clips from an *in situ* movie acquired as the surface develops roughness during ion erosion, using the SEM to image at the same time as the FIB etches (5 nA @ 30 keV). The FIB and SEM beams are both rastered out of sync to minimize interference, however some noise is introduced as straight horizontal lines and bands. Since the FIB produces secondary electrons, the current of the SEM (1.6 nA @ 5 keV) has to be much greater than typical SEM imaging so that the secondary electron image corresponds to where the SEM is rastering [34]. The SEM beam is deliberately rastered partially off the edge of the FIB crater to provide a constant frame of reference, such as the dirt particle indicated by the arrow. Processing is commonly >1 h, during which samples experience drift at the nanoscale; thus a frame of reference is necessary to monitor ripple evolution and motion. Since these ripples are produced with an ion angle of incidence of 60°, the SEM movie provides a view only 8° from normal to the surface. The slight inclination of the SEM view means vertical dimensions are foreshortened 1% compared to horizontal measurements. (Movie is supporting data available online at stacks.iop.org/JPhysCM/21/224013.)

Figures 5(g) and (h) are still shot SEM images acquired normal to the surface [33] after *ex situ* FIB etching a crater to depths of 4000 and 5700 nm, with doses of 13 and $21 \times 10^{18}$ ions $cm^{-2}$, respectively. In figure 5(g), the ripple wavelength is ~280 nm, but closer to the leading edge of the crater the wavelength is ~420 nm. Upon further erosion, the wavelength grows to 310 nm (figure 5(h)), however, the 420 nm wavelength persists for the near-edge ripples. Two-step processes [12, 46, 57] have indicated these near-edge ripples also align with three-dimensional boundaries.

SEM can measure etch depths as well as ripple growth. A 2-tilt method for metrology of etch craters has been developed by including FIB spot burns at the tops and bottoms of craters, such as visible in figures 1(e) and (f). The mathematical details are described elsewhere [33]. With a measure of crater depth and size, the aspect ratio can be calculated, as well as the decaying yields in figure 1(b). Figures 5(i) and (j) plot the ripple wavelength as a function of dose, which is usually plotted for many materials [45, 72], and as a function of aspect ratio. Data in these plots only include FIB etching at 60° angle of incidence, and chemically enhanced yields due to water are also included. The *in situ* SEM movie datapoints are also contrasted to *ex situ* data. The ripple wavelength growth correlates better to aspect ratio than dose, and even enables chemical-enhanced etching to better fit the correlation. It is noted that chemical-enhanced ion sputtering is often credited with mitigation of surface roughening [14, 80–82], however during fast ion etching it also appears chemistry can be controlled to enhance ripple growth, too [33, 37]. The added energy provided by the SEM during the *in situ* movie can also enhance ripple growth [34]. However, this electron beam enhancement of ripples occurs with a drop in yield, opposite to chemical-enhanced yields. If the SEM beam is not on, and there is no water vapor, the yield at 60° starts at >6, dropping to an averaged 5.6 at an aspect ratio of ~0.2 (figure 5(g)), and to 4.7 at an aspect ratio of ~0.29 (figure 5(h)). During the SEM movie, however, the averaged yield drops to 3.4 by a depth of 6400 nm and aspect ratio of only 0.23. In both the cases of chemical and electron beam modified ion sputtering, the ripple growth is attributed to redeposition [34], and the well-regulated spacings of the ripples is a declaration of the control and reproducibility of the redeposition process.

Even though redeposition is controllable and reproducible, it is often avoided for ripple modeling based on Bradley/Harper theory [25]. Redeposition is a practical, albeit sometimes undesirable, concern in FIB and/or processing of surface features of high aspect ratio. With yields decaying for aspect ratio as low as 10% (figure 1), redeposition will affect local yield inside each trough between nanometer-scale ripples and dots. Some modeling theories incorporate redeposition [55, 77, 78, 49, 79], but the high flux, high aspect

ratio, and boundary conditions of FIB processing do not easily adapt to present models. Kustner *et al* [77] models redeposition to match ion-induced topologies on Beryllium, which are experimentally monitored by scanning tunneling microscopy (STM) with a spatial pixel resolution >40 nm. A more recent study of FIB etching Be has shown 2D dot arrays can form spaced <30 nm [37]. However, even FIB processing is not immune to effects of material inhomogeneity, such as different crystal orientations (see figure 5(d) of [37]) or (grain) boundary conditions (see figure 5(a) of [37]). Some of the larger topologies observed by Kustner [77] may be influenced by material inhomogeneities. The effects of boundary conditions that arise due to inhomogeneities involve complex alterations to modeling, such as the rotation of ripples to align parallel to boundaries [12, 37], and the doubling of dot periodicity near Be grain boundaries [37]. It is likely that surface inclination changes near boundaries due to alteration of the local yield, but in practice it is unclear whether this leads or follows the dramatic changes to self-organizing topologies. It is also likely that the redeposition term dramatically changes near boundaries.

An important addition to ripple modeling is a dampening term [78, 49] that may account for redeposition but also help explain the formation of hexagonal arrays of dots. An extension of such dampening has recently modeled the transformation from dots to 1D ripples [79]. However, again the FIB processing of polycrystalline Be shows the dot array is not exactly hexagonal and is easily influenced by a grain boundary hundreds of periods away. But more important than enacting or exposing boundary conditions, FIB processing has a strong chemical component due to the state-of-the-art use of Ga+ ions. (Kustner's work evoked the more ideal case of Be ions to erode a Be target.) The FIB's high current quickly results in a substantial concentration of Ga, whether a normal or grazing incidence is applied. Phase diagrams between Ga and most target materials allow for intermetallic phase formation or even room temperature liquids. 'Creeping crud' is commonly observed when FIB erodes transition metals [17], although this phenomenon appears separate from ripple formation in actinides such as Uranium, where the ripples are dominated by the different yields for different grain orientations. Movies of FIB etching heavy metals (e.g. Bi) are dominated by liquid migration out of deep pits and the formation/dissolution of liquid drops at the tops of dots [50]. Even when incidental ions are inert, erosion of compound semiconductors typically leaves a chemically affected surface enriched with the low-melting-temperature metallic species [55]. The FIB not only locally alters chemistry but also introduces a strong local charge field that produces different redeposition kinetics for departing positive and negative species. The redeposition effects are well controlled and reproducible during FIB processing of self-organizing topologies, however the effects of chemistry and boundary conditions require additions to present ion erosion models.

In addition to observing ripple wavelength growth beyond saturation steady state [72], the SEM movie monitors the ripples moving southward and away from the ion inclination, akin to waves pushed downwind. During the SEM movie, the ion dose rate is $\sim 1 \times 10^{16}$ ions cm$^{-2}$ s$^{-1}$, and the wavelength increases from 250 to 290 to 370 nm, at doses of 5, 10, and 33 $\times 10^{18}$ ions cm$^{-2}$, respectively. Although most of the wavelength growth is at the lower doses, these wavelengths all exceed the $\sim$220 nm saturation reported [72] to occur at a dose of only 1–2 $\times 10^{18}$ ions cm$^{-2}$. Wave motion appears quite linear with dose: $\sim 1$ $\mu$m per 4.8 $\times 10^{18}$ ions cm$^{-2}$. This motion, which is more accurately monitored by SEM after wavelength exceeds 200 nm, is significantly greater than some motion naturally expected due to the ripple growth rate. The motion is measured after accounting for the additional geometrical motion of the pit bottom itself moving southward as the FIB creates an inclined pit (see details in [34]). However, a rationale for linear wave motion is not evident. Etch rate is not constant at the bottom of the pit; and the wavelength is neither constant nor linearly increasing with dose. A similar SEM movie of ripple motion on single crystal sapphire also appears linear with dose, albeit at less than half the speed ($\sim 1$ $\mu$m per 12 $\times 10^{18}$ ions cm$^{-2}$.) Other models for wave motion have even considered that ripples could move upstream rather than downstream [81, 82], however, a geometric analysis of the eroding surface requires judicious metrology. Even with high current FIB, self-organizing nanostructures evolve in minutes or hours, during which sample drift of several nanometers is likely. Also the charge field changes as a FIB pit deepens, requiring additional metrological adjustment of the frame of reference (see movie data of figure 5 (available at stacks.iop.org/JPhysCM/21/224013)). The upstream side of a ripple is being eroded with the ion beam nearly normal, whereas the downstream side of the ripple is eroded by ions at grazing incident. Thus the downstream side experiences a higher erosion yield. However, a simple asymmetric sawtooth model for ripples (similar to figure 7(b) and experimentally observed for many materials [19, 39]) will have a larger surface area on the downstream side of the ripple. Also the downstream side of the ripple sees a smaller projected current from the inclined ion beam. Consequently, the overall current density at a point on the downstream side of the ripple is lessened geometrically faster than its yield is enhanced. The upstream face of the ripple etches faster; therefore ion etching causes ripples to move downstream. This geometrical effect plays a role in practical micromachining by FIB, too. Grazing incident machining can enhance the yield; however, such angle spreads the FIB current over a larger area. For a given focused current density in a FIB probe, scanned over a pattern to be etched, it is faster to finish the process with the FIB etching normal to the surface.

Self-organized ripples are not perfect, and line defects are common. The SEM movie also shows the motion of line defects amongst the ripples, and these defects move thrice the speed of surrounding waves. Some defects can appear and disappear, and as ripples grow larger the defect density naturally drops. However, defects appear quite robust, and these wave defects do not always exhibit energetically logical line defect reactions. An extrinsic fault line (figure 5(a)) shrinks, but rather than annihilating itself, it breaks the neighboring ripple line to jump forward in figures 5(b) and (c),

and then regrows in length in figure 5(d). The process repeats to figure 5(g), and continues to repeat (shown elsewhere [34]). In another location, the opposite ends of two line defects are in close proximity and should energetically annihilate. But instead they jump in tandem, faster than the surrounding waves [34]. A model of wave motion including redeposition downstream can help rationalize defect motion. The tops of ripples are preferentially eroded by an ion beam, which is impinging at a glancing angle. The ends of the extrinsic fault are similarly affected and preferentially erode away. It is energetically expected that the extrinsic fault should erode away and completely disappear. However, the sputter-etched material also becomes a source material downstream. Thus when more erosion occurs at edges, this becomes a greater source of redeposition. The excess erosion of the two ends of the extrinsic fault line provides excess redeposition downstream. This enables a new line defect to be created downstream, as the extrinsic fault is eroded away. However, it would be energetically unfavorable to just interject a second extrinsic fault. Thus the extrinsic fault is moved downstream by breaking the adjoining ripple lines, creating two opposing 'dislocated' ripples as an intermediate. The double dislocated intermediate still provides two ends, which are eroded at a faster rate than the rest of the ripples. This becomes the relative motion that makes the defect wave move faster than full waves. The extrinsic fault jumps ahead 3 wave spacings as the dose is increased from 13 to 16.2 $\times$ $10^{18}$ ions $cm^{-2}$, or $\sim$1 jump per 1 $\times$ $10^{18}$ ions $cm^{-2}$. With a wavelength of $\sim$300 nm, this jumping of defects is several times faster than the full wave motion; thus over a big area with many defects, the defects can account for much of the wave motion (but not all of the motion).

The discussion of ripple motion in the earlier sawtooth model, as well as the optimization of micromachining speed by FIB normal to the workpiece, need to include a factor of redeposition, too. In some micromachining geometries, redeposition can be minimized by ion beam inclination; however, in the case of a pit, the angle of incidence increases the redeposition effect (figure 1). Similarly the trough between two ripples may be defined as an elongated pit, in which redeposition depends on angle of incidence and aspect ratio. When ripples move downstream during erosion, redeposition affects ripple speed, however, the role of redeposition remains unclear. Redeposition is expected to accumulate on the upstream side of the ripple, and if it is sufficient, then it would enable the erosion speed of the downstream side to become the greater and thus ripples should move upstream. Experimentally, however, the ripples are observed moving downstream. This same effect of redepositing onto the upstream side of the next ripple would also cause a decrease in ripple wavelength, whereas experimental results indicate increased redeposition causes ripple wavelength to grow. Redeposition appears to encourage ripple motion, and especially line defect motion, but redeposition's primary role is to affect growth of ripple wavelength.

Figure 5(k) is an SEM image depicting two erosion pits prepared by FIB. In the left case the FIB is incident at 60° and produces sputter ripples as discussed earlier, and in a mode the same as for a static beam (i.e. independent of the computer-controlled scanning parameters of the FIB). However, when a FIB is used, there is also the possibility to take advantage of the FIB tool technology and computer control. For both cases, the FIB is scanned vertically, starting at the left, to show the scan direction of the FIB is not critical to ripple orientation. In the right erosion pit, the FIB beam is patterned with a negative overlap between horizontal lines so as to produce parallel pits (trenches) spaced exactly 500 nm. In this second case the FIB beam is incident normal to the surface, enabling better precision and minimizing effects of self-organization (in diamond). A roughened bottom of a pit, whether intentionally patterned or self-organized, is predicted to etch faster than a flat bottom crater [1, 8]. But for FIB processing of deep pits, the flat bottom craters maintain more efficient etching and scan patterns are usually optimized to keep the bottom of the pit flat. (See earlier discussion of negative overlap in section 2.1 and [4, 33].) During this intentional production of patterned ripples, the negative overlap was chosen such that the roughness does not dramatically alter the etching efficiency, thereby ensuring pattern precision and control. Although different angle of incidence results in a different yield for the two cases (3.3 and 2.3 for left (60°) and right (0°), respectively), the energy, current, and dose of the FIB are the same (30 keV, 5 nA, and 14 $\times$ $10^{18}$ ions $cm^{-2}$, respectively). The self-organized ripples are quite uniform and reproducible, but their wavelength ($\sim$280 nm) represents a discrete processing condition and aspect ratio as the ripples evolve. Conversely, the patterned ripples achieve their wavelength at low flux and maintain the prescribed 500 nm wavelength throughout the entire process. If the goal is to produce ripples that are upwards of 10–1000 nm in wavelength, then it becomes possible to consider intentionally placing the arrangement of the erosion ripples through FIB patterning rather than allowing them to self-organize.

Ripples grow, but can they be grown smaller [37, 50]? Although figure 5(k) indicates FIB patterning of straight ripples may provide more control than self-organized nanoscale modulations, the FIB resolution and control remain impractical for patterning subnanometer-spaced ripples. (Note the He ion microscope does not sputter etch at its 100pm resolution [71].) Thus a big static beam is as likely as a FIB to produce subnanometer-scale ripples. However, a FIB tool offers more flexibility: in stage, in sample 3D geometries, in beam control, and with add-on's such as local chemical enhancement, micromanipulators and 2nd beams, all of which can optimize ripple processing [19]. Furthermore, the site-specific placement of subnanometer structures is as critical as creating them.

One site-specific function of FIB is the practice of making TEM cross-section samples. TEM sample preparation and self-organized modulations are typically unrelated sciences, however, ripples have often been observed as an artifact of ion beam processing of TEM samples, ranging from un-oriented ripples on semiconductors and glasses to different grain orientations having different ripples for metals from Be to Bi [58, 4, 37]. The advent of FIB for processing TEM

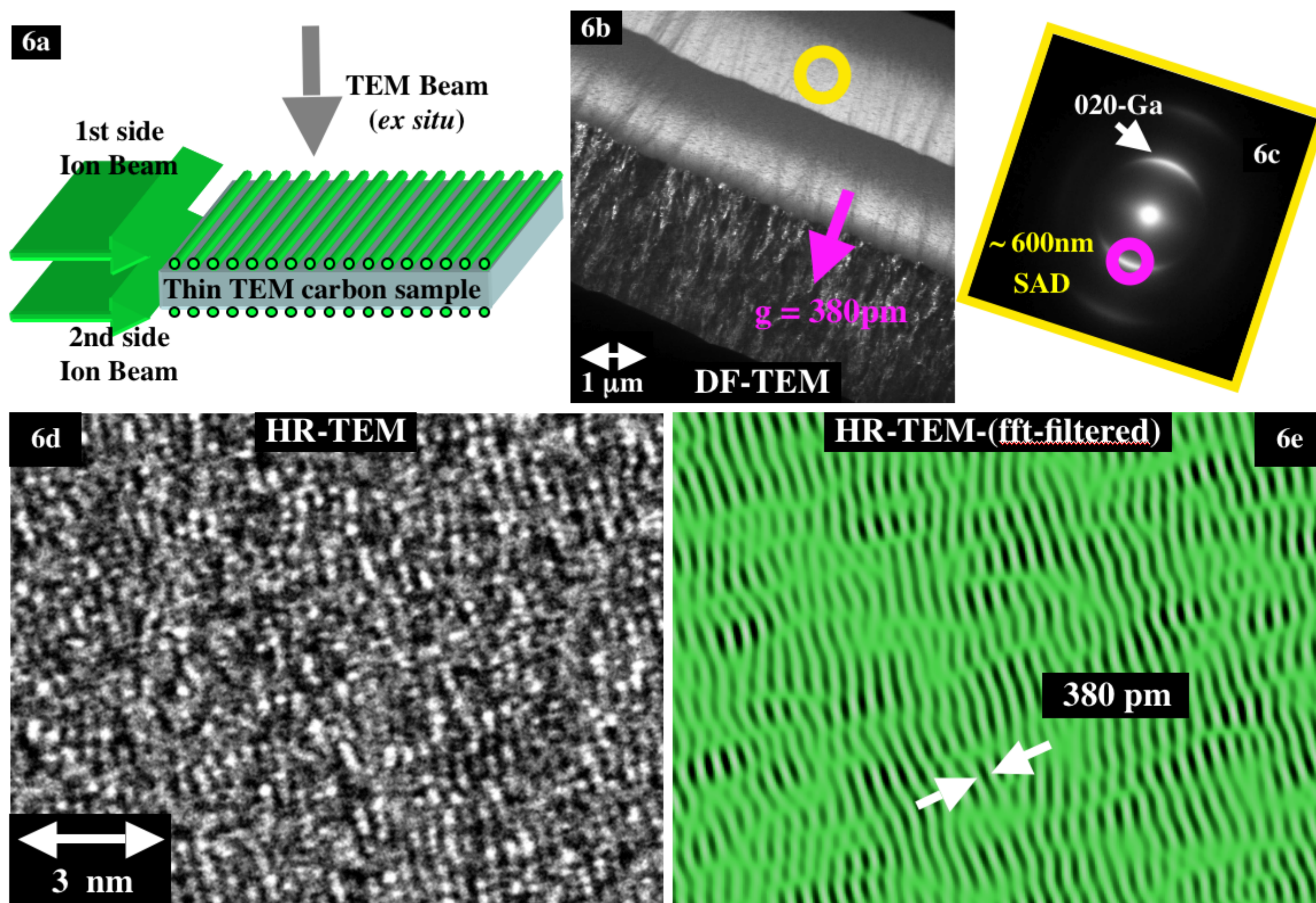


**Figure 6.** FIB preparation of TEM samples involves final polishing step with FIB inclination at 90° in schematic (a). A high angle encourages ripple growth for many materials, but the geometry for preparation of a HR-TEM sample requires the finished surface be (near) atomically flat. Thus ripples grow to only subnanometer scale. Also the Ga ion beam contaminates the surface of TEM samples, and at 90° this contamination is confined to nearest the surface, as well as being a larger concentration of the top monolayer. At the extreme of erosion, when the FIB has finished polishing, it self-deposits while self-organizing. (Such quantized picostructures may be grown on tops of pedestals using other ion species.) ((b), (c)) Dark field TEM and selected area diffraction show the subnanometer ripples are well ordered over millions, but confined to grow on Carbon-based layers of a CVD-SiC–C multilayer [57, 34]. ((d), (e)) High resolution TEM can image the picostructures, but they appear akin to astigmatism and may easily be missed without fft-filtering the amorphous carbon substrate.

samples often attributes FIB precision to the mitigation of surface topologies [4, 17]. Yet whether a large static ion beam or a FIB is applied to TEM sample preparation, it is common for a final processing step to evoke an ion beam inclination approaching 90.0°. Thus a geometric controversy is occurring when considering the two separate functions. For the case of processing self-organized ripples the approach of 90° incidence generally is to provide a larger modulation, both in wavelengths and amplitudes of ripples and/or steps [25, 39]. Conversely, ion milling of a TEM sample, and especially FIB-TEM-prep, applies the 90.0° incidence with a goal to produce near-atomically-flat surfaces for optimal High Resolution TEM imaging [37, 50]. In practice, the 90° ion incidence erodes the tops of ripples faster than it produces them, and a modern TEM sample can be made essentially atomically flat over several microns [4, 17, 57]. However, the surface phenomena wanting to ripple the surface are still present and can be optimized in the same conditions as applied for TEM sample preparation.

Two other issues are associated with FIB preparation of TEM samples in addition to the geometric conflict at 90°. The use of a Ga ion beam results in some Ga contamination of TEM samples. Often this amount can appear insignificant in an HR-TEM image, yet in other cases reactions between Ga and transition metals can lead to new phases present on TEM samples [17]. When the FIB is incident near 90.0°, the Ga concentration can be significantly increased in the top few atomic layers of the sample. Secondly, the final FIB polishing steps for TEM-prep are reaching a condition where the etch rate (due to geometry and precision) is intentionally dropping to 0 (figure 6(a)). All ion beam processing involves some of the incident ion beam being deposited (and/or implanted); however, sputter etching is generally a condition where more atoms are etched off than deposited and this generally prevents significant contamination build-up. However, the final FIB polishing of a TEM sample wants to stop the sputter etching, and at the last instance the topmost layer of the sample will be the most heavily contaminated with the depositing ion species. For a Ga-FIB, such Ga atoms do not subsequently vaporize off the surface. Although an ideal aspect ratio = 0 for atomically flat prepared surfaces will mean redeposition can be negligible, suddenly deposition itself is occurring. As atoms deposit, the

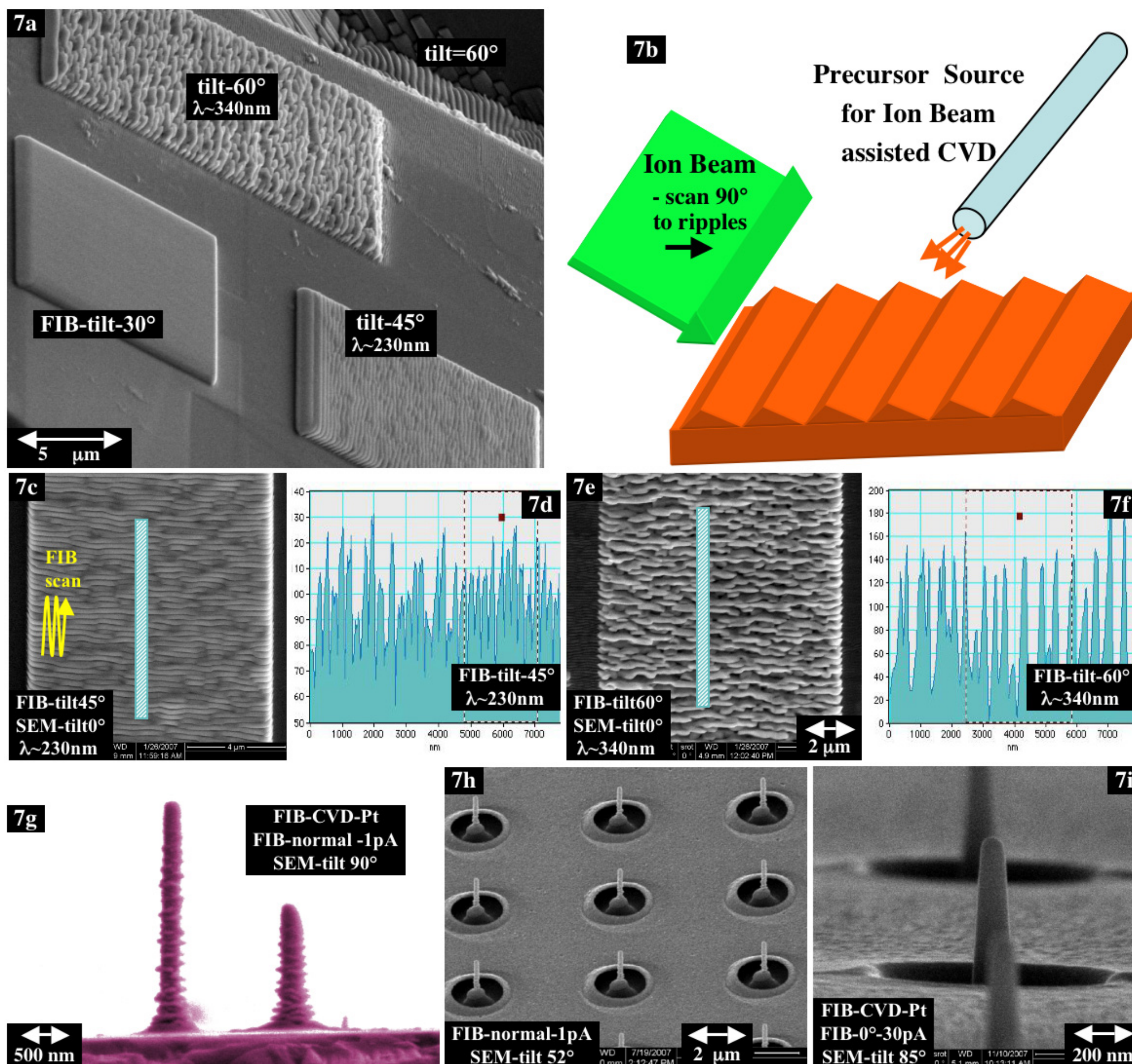


**Figure 7.** (a) SEM image of carbon pads grown by FIB-CVD, with ion beam at inclinations of: 30° tilt to produce a smooth surface, 45° a set of 1D ripples, and 60° two-dimensional steps (akin to erosion angles [39, 50]). (b) Schematic shows FIB scan is intentionally normal to ripples (i.e. ripples relate to inclination angle and are not caused by FIB scanning.) ((c), (e)) SEM at normal view of pads grown at 45° and 60°, to enable metrology of wavelengths ((d), (f)) of ∼230 nm and ∼340 nm, respectively. Ripples grown on top of pads have more engineering utilities than erosion ripples at bottom of pit (in background of (a)). (g) Colorized SEM views ripples along sides of Pt pillars grown by FIB-CVD. (h) Pillars and ripples are reproduced in seconds, although beam spread produces a diameter well in excess of the <10 nm ion beam. (i) FIB can also etch away surface ripples to sharpen tips.

energy of the ion beam passing over the surface also self-organizes the surface at the picometer scale.

Figures 6(b) and (c) are TEM data, dark field (DF) image and selected area diffraction (SAD), respectively, acquired of a sample prepared by FIB at ∼90° as shown in figure 2. Details of FIB processing to prepare TEM specimens are discussed in several textbooks [4, 17, 67] and TEM courses [58], and the preparation of these specimens from CVD multilayers of C and SiC on fibers is evaluated earlier [50, 57]. Two separate experiments [57] have been conducted to have the surfaces energized by FIB etching normal to the interface of the coatings and at ∼40° inclination to the interface, with figures 6(b) and (c) acquired for the latter. In order to establish the long-range reproducibility of the ion processing, a region extending >20 $\mu$m is prepared, all appearing similar to the few microns imaged in figure 6(b). The circle in figure 6(c) indicates the relative size and effective placement of the objective aperture used to produce the DF image of figure 6(b). The location of the millions of ripples spaced 380 pm become highlighted as bright swaths extending along the carbon-rich portion of the multilayer coatings. The circle in figure 6(b) represents the effective size and location of the SAD aperture used to provide the SAD pattern in figure 6(c). Diffraction establishes the exceptional long-range order of the

modulation, and SAD patterns from various regions establish the location of the modulations only on the carbon-rich zones. As well as providing a measure of the modulation wavelength, the electron diffraction establishes the orientation of the ripples parallel to the multilayer interfaces, and this orientation remained independent of the FIB's inclination to the interface [57].

Figure 6(d) is a high resolution micrograph (HR-TEM) presenting phase contrast acquired from the carbon-rich portion of the CVD coatings. Figure 6(e) has been image processed from figure 6(d) to selectively filter the ripples so as to more readily view their location. The TEM image consists of phase contrast from the carbon comprising the majority of the thin lamellae as well as the frontside and backside FIB-processed surfaces. Thus image processing (removal) of much of the phase contrast due to the carbon improves visibility of ripples. This FFT processing is akin to the use of the selective objective aperture placed upon the SAD pattern of figure 6(c) to produce the DF image of figure 6(b). (Complementary BF and DF images of different $g$-vectors can similarly negate visibility of the ripples in TEM imaging [37].) Similarly, in the schematic of figure 6(a), the amorphous carbon that makes up the majority of the TEM sample is subtracted, so as to leave an image of just ripples of Ga on the frontside and backside surfaces. This single set of rows of atoms on a surface may be referred to as a textured 1-and-1/2-dimensional crystalline film.

HR-TEM is useful for observing structures at atomic dimensions; however, the imperfect natures of lenses and operators mean that an image commonly has astigmatism included. When imaging amorphous materials, where no periodicities are presumed present in all directions, any nonuniformity observed with directionality is treated as astigmatism and attempts are made to correct it. Thus the ripples observed in figure 6(d) initially cannot be distinguished from an artifact of astigmatism. Since HR-TEM can also provide crystalline lattice images, a nearby crystalline region was used to optimize imaging conditions and assure that astigmatism is not present [37]. Although a visual confirmation, the HR-TEM image of the ripples cannot quantify the long-range order as the field of view of this type of image is good to only 10's of nanometers (i.e. ∼100 ripples). However electron diffraction in a TEM is optimized for the study of spacings much smaller than those between atoms in crystals (sub-Angstrom), and electron diffraction easily scales to sample regions of many microns (e.g. millions of ripples in figure 6(c)).

The subnanometer ripples of Ga that form on the surface of a TEM sample are naturally quantized to a spacing representative of Ga interatomic spacings (e.g. 380 pm). The spacings along a ripple are natural to Ga, and the spacings between ripples are natural to Ga. However, a 2D periodic lattice does not form. In this case, the surface diffusion component of ripple theory [2, 25, 26] does not enable sufficient long-range order to crystallize the Ga during the energetic exposure at 90°. It is noted that Ga precipitates are a common artifact on TEM specimens prepared by FIB, and Ga trapped on surface steps in the SiC portion of these TEM specimens do exhibit crystalline lattice fringes. Picoripples are on the carbon layers but not on the SiC in figure 6(b), but this is not unusual as different materials exhibit different ripple behavior [2, 5, 12]. The carbon surface plays an important physical and/or chemical role, but it is not the carbon that is self-organizing to form 340 pm ripples but rather the Ga-380 pm spacing. The orientation of the ripples is controlled by the orientation of the incident ion beam, and by boundary conditions such as interfaces within the sample. These ripples self-organize over many millions, and their strong orientation and quantization over long range are evident in SAD diffraction patterns. The TEM sample involves 2 surfaces, and subnanometer ripples exist on both sides. However, it is possible to have an ion beam (not necessarily focused) pass over only the top surface of a pedestal and lead to the same deposition of a non-volatile ion species, and whereby the orientation of the quantized ripples is controlled by the orientation of the ion beam.

If ripples grow, can they be grown up instead of down? Ion erosion ripples are actually being grown downward below the original surface (figure 5(g)); and especially in the case of FIB, the production of self-organized structures at the bottom of a pit may have limited utility (although imprinting may reverse them to the top of a pedestal, possibly for Discrete Track Recording) [19, 37]. If the reverse reaction can be controlled so precisely to capture deposition during erosion and grow picostructures, than can erosion be controlled during a deposition process? FIB-CVD is commonly used to grow site-specific pads, and in figure 7(a) carbon pads are grown but with modulations forming on surfaces controlled by the FIB angle of incidence. Figure 7(b) presents a schematic of the ion beam inclination with local gas injection leading to a modulated surface for FIB-CVD growth. For a FIB inclination near normal, the pad grows with a flat surface; at an inclination of 45° one-dimensional modulations form in the pad surface; and at ∼60° the modulations appear 2D. This is akin to how erosion angles influence 1D ripples versus 2D steps [39]. Figures 7(c) and (e) are SEM images acquired normal to the carbon pads, and the wavelength of modulations are quantified in figures 7(d) and (f) as 230 nm and 340 nm for the 45° and 60° growths, respectively. One concern of using a FIB for ion beam processing is that the scan pattern of the FIB may alter the pattern of the modulations. With controlled scanning, any influence of the scan pattern appears preventable [37]. For these carbon growths, the scan pattern of the FIB was rotated 90° with respect to the orientation of modulations with no impact. The orientation of modulations relate only to ion beam angle of incidence. Modulation also depends on many growth parameters such as current, pressure and scan rate [50], and modulations also appear to extend below the top surface providing 3D modulations. Growth is traditionally controlled by chemistry and epitaxy, however ion beam processing in the hard drive industry already evokes modulations and interacts with pre-patterned modulations (texture scratches) [83] to produce magnetic storage structures spaced only a few nanometers. FIB-CVD processing of self-organized ripples on the sides of Pt pillars (pagodas in figure 7(g)) is fast and reproducible (figure 7(h)), but modeling is complex to evaluate the implantation cascade

and subsequent secondary emission at the sides that activate ripple growth. FIB etching can also remove ripples from sides of tips (figure 7(i)), if appropriate for field emitting nanoscale neutron sources [84, 85]. The complexities of ion-assisted-CVD in 2D and especially FIB-CVD in 3D require further characterization of experiments and modeling [86, 87]. Carbon pad growth is viable by the SEM (EBAD—electron beam assisted deposition), too. Thus 2-beam processing [19] can have the ion beam angle, current, site-specificity, etc all independent of the growth.

## 3. Conclusions

On a free energy diagram, the reverse reaction is always happening; for macroscopic systems it can be statistically irrelevant, however at the nanometer and picometer scale it can be paramount. The reverse reaction of erosion is deposition, often occurring as redeposition, which is a function of aspect ratio, during ion beam processing. When energized by ions, two-dimensional surfaces naturally erode to develop 3D topologies, with several parameters (energy, angle, chemistry, electron beam, etc) enabling modification of these self-organizing nanostructures. Conversely, during ion-assisted deposition, the reverse reaction of erosion can be evoked to modulate growth surfaces. However, the aspect ratios of these developing surface modulations impose boundary conditions for subsequent impinging ions. The purpose of FIB processing is to impose site-specificity, hence 3D geometric boundary conditions occur by design, and redeposition can be either a predicament or a productive processing parameter. Redeposition causes yield to drop with increasing aspect ratio in a deepening pit. Redeposition enables growth of self-organized nanostructures on diamond to wavelengths upwards of 500 nm, and an SEM movie watches these erosion ripples move downstream (~2 $\mu$m per dose of $1 \times 10^{19}$ ions cm$^{-2}$). Redeposition can cause holes through amorphous membranes to shrink to a few nanometers or completely close. For a hole of low aspect ratio through a thin membrane, however, ion erosion only further opens the hole. But turn a very thin membrane over and backside erosion can evoke bottomside redeposition to close pits. Topside sloping sidewalls caused by beam tails mean less redeposition occurs during backside erosion and hole closure is slowed. The lack of hole closure during near-field erosion indicates that redeposition is a source term due to aspect ratio only within the hole itself. Thus it appears redeposition can be averted if aspect ratio is avoided; if the surface is kept 2D-flat during ion beam processing. When processing atomically flat surfaces, such as for preparation of high resolution TEM samples, ion impingement at an inclination of 90.0° enables ion-energized deposition itself to self-organize millions of ripples quantized to the 380 pm of Ga from the ion beam. These ion-beam-controlled ripples, more than one thousand times smaller than the nanostructures grown on diamond, are defined picostructures.

Can a FIB etch a 1 nm diameter hole? The question is really, how deep [59]? The answers are implantation cascade, aspect ratio and redeposition. More than 100 small holes through a thick (400 nm) membrane all closed during ion erosion exposure; however, >100 holes through a thin (20 nm) membrane all opened larger. Pits (non-penetrating holes) of high aspect ratio all closed, both by frontside and backside erosion. The limit for aspect ratio is 5-to-20, depending on how much topside rim erosion to larger diameters is acceptable. But redeposition starts even when aspect ratio of a pit or hole is 10%. I.e. eroding a 1 nm hole starts experiencing redeposition when it is made through a membrane more than one atom thick. Alternatively, etching a hole through a membrane only 5–10 nm thick enables the high energy ions to penetrate and bottomside sputter, explosively opening a bottom-up hole with a minimum diameter of 20–30 nm that matches the implantation cascade for 30 keV Ga ions. Yet backside erosion of a slightly thicker membrane enables bottomside redeposition to close pits, encapsulating nanometer-scale structures with potential confinement as 3D arrays of dots. Direct-write etching of a smaller diameter hole requires the smaller implantation scatter of lower energy ions, as well as thinner membranes to limit aspect ratio and both topside and bottomside redeposition.

FIB processing of structures, both self-organizing topologies and nanometer-scale apertures, can be as uniform and reproducible as for static ion beam processing. In addition, FIB is fast and efficient so that designs can be easily tested and modified. However, the complexities of redeposition, which are aggravated by the chemical changes and boundary conditions evoked during FIB processing, require further development of the dampening terms in predictive models of ion erosion. The FIB, and especially the recent 2-beam FIB/SEM, enables *in situ* metrology of self-organizing topologies. One intriguing observation is the motion of defects, even for conditions that energetically appear unfavorable. This defect motion supports redeposition as a major factor in the evolution of eroding surfaces, and future metrology of these defects will aid both predictive modeling and control of topologies. Future development of multi-ion source FIBs will help reveal what effects are independent of Ga chemistry; and continued improvement of atomistic modeling [52] will further the understanding of backside erosion and bottomside redeposition when processing small 3D structures.

## Acknowledgments

This work was performed under the auspices of the United States Department of Energy by the Lawrence Livermore National Laboratories under contract of No. DE-AC52-07NA27344. LLNL-JRNL-405668. The author is grateful to Luis Zepada-Ruiz for thoughtful discussions and exciting and illuminating modeling results.

## References

[1] Sigmund P 1973 *J. Mater. Sci.* **8** 1545
[2] Chason E *et al* 1997 *Appl. Phys. Rev.* **81** 6513
[3] Nordlund K, Ghaly M and Averback R S 1998 *J. Appl. Phys.* **83** 1238
[4] Giannuzzi L A and Stevie F A 2005 *Introduction to FIB* (New York: Springer)
[5] Aziz M J 2006 *Matematisk-Fysiske Meddelelser/udg. af Det Kongelige Danske Videnskabernes Selskab Ion'06 Proc.* vol 52, ed P Sigmund, p 187
[6] Williams J S and Poate J M (ed) 1984 *Ion Implantation and Beam Processing* (New York: Academic)

[7] Appleton B R, Holland O W, Narayan J, Schow O E, Williams J S, Short K T and Lawson E 1982 *Appl. Phys. Lett.* **41** 711
[8] Sigmund P 1969 *Phys. Rev.* **184** 383
[9] Harper J M E, Cuomo J J and Kaufman H R 1982 *J. Vac. Sci. Technol.* **21** 737
[10] Averback R S, Diaz de la Rubia T and Benedek R 1988 *Nucl. lnstrum. Methods* B **33** 693
[11] Colligon J S 1991 *Mater. Sci. Eng.* **139** 199
[12] Cuenat A and Aziz M J 2002 *Mater. Res. Soc. Symp. Proc.* **696** N2.8
[13] Chen H H, Urquidez O A, Ichim S, Rodriguez L H, Brenner M P and Aziz M J 2005 *Science* **310** 294
[14] Orloff J, Utlaut M and Swanson L 2003 *High Resolution FIB and its Applications* (New York: Kluwer Academic/Plenum)
[15] Melngailis J 1987 *J. Vac. Sci. Technol.* B **5** 469
[16] Stevie F A, Shane T C, Kahora P M, Hull R, Bahnck D, Kannan V C and David E 1995 *Surf. Interface Anal.* **23** 61
[17] Mayer J, Giannuzzi L A, Kamino T and Michael J 2007 *MRS Bull.* **32** 400
[18] Volkert C A and Minor A M 2007 *MRS Bull.* **32** 389
[19] MoberlyChan W J, Adams D P, Aziz M J, Hobler G and Schenkel T 2007 *MRS Bull.* **32** 424
[20] Facsko S, Dekorsy T, Koerdt C, Trappe C, Kurz H, Vogt A and Hartnagel H L 1999 *Science* **85** 1551
[21] Cuerno R and Barabási A-L 1995 *Phys. Rev. Lett.* **74** 4746
[22] Langford R, Nellen P M, Gierak J and Fu Y 2007 *MRS Bull.* **32** 417
[23] Carter G and Vishnyakov V 1996 *Phys. Rev.* B **54** 17647
[24] Giannuzzi L A *et al* 1997 Specimen preparation for TEM *Mater. Res. Soc. Symp. Proc.* **480** 19
[25] Bradley R M and Harper J M E 1988 *J. Vac. Sci. Technol.* A **6** 2390
[26] Erlebacher J, Aziz M J, Chason E, Sinclair M B and Floro J A 1999 *Phys. Rev. Lett.* **82** 2330
[27] Tersoff J 1996 *Phys. Rev. Lett.* **76** 1675
[28] Gray J L, Atha S, Hull R and Floro J A 2004 *Nano Lett.* **4** 2447
[29] Aziz M J, Floro J A, Mayer S G and Umbach C C (ed) 2007 Nanoscale pattern formation *Mater. Res. Soc. Symp. Proc.* **1059E**
[30] Ziegler J F, Biersack J P and Littmark U 1985 *The Stopping and Range of Ions in Solids* (New York: Pergamon)
[31] SRIM program www.srim.org
[32] Lugstein A, Brezna W, Hobler G and Bertagnolli E 2003 *J. Vac. Sci. Technol.* A **21** 1644
[33] MoberlyChan W J, Felter T E and Wall M A 2006 *Microsc. Today* **14** 28
[34] MoberlyChan W J and Schalek R 2007 Nanoscale pattern formation *Mater. Res. Soc. Symp. Proc.* **1059E** KK1–7
[35] Matthes A, Schmidl F, Barholz K-U, Elschner F, Schneidewind H and Seidel P 1995 *Supercond. Sci. Technol.* **8** 676
[36] Schenkel T, Radmilovic V, Stach E A, Park S J and Persaud A 2003 *J. Vac. Sci. Technol.* B **21** 2720
[37] MoberlyChan W J 2006 Self assembly of nanostructures aided by ion or photon-beam irradiation *Mater. Res. Soc. Symp. Proc.* **960E** N10–2
[38] Russell P E, Stark T J, Griffis D P, Phillips J R and Jarausch K F 1998 *J. Vac. Sci. Technol.* B **16** 2494
[39] Adams D P, Vasile M J, Mayer T M and Hodges V C 2003 *J. Vac. Sci. Technol.* B **21** 2334
[40] Broers A N, Hoole A C F and Ryan J M 1996 *Microelectron. Eng.* **32** 131
[41] Biance A-L *et al* 2006 *Microelectron. Eng.* **83** 1474
[42] Zhou J 2006 *Int. J. Precis. Eng. Manuf.* **7** 18
[43] Adams D P, Patterson N, Hodges C, Vasile M, Michael J and Kotula P 2008 Focused ion beams for materials characterization and micromachining *Mater. Res. Soc. Symp. Proc.* **1089E** Y1–4
[44] Kempshall B W, Schwarz S M, Prenitzer B I, Giannuzzi L A, Irwin R B and Stevie F A 2001 *J. Vac. Sci. Technol.* B **19** 749
[45] Mayer T M, Chason E and Howard A J 1994 *J. Appl. Phys.* **76** 1634
[46] Ichim S and Aziz M J 2005 *J. Vac. Sci. Technol.* B **23** 1068
[47] Brown A D, Erlebacher J, Chan W L and Chason E 2005 *Phys. Rev. Lett.* **95** 056101
[48] Mayer T M, Adams D P, Vasile M J and Archuleta K M 2005 *J. Vac. Sci. Technol.* A **23** 1579
[49] Castro M, Cuerno R, Vazquez L and Gago R 2005 *Phys. Rev. Lett.* **94** 016102–05
[50] MoberlyChan W J 2007 *Microsc. Microanal.* **13** 598
[51] Diaz de la Rubia T, Averback R S, Benedek R and King W E 1987 *Phys. Rev. Lett.* **59** 1930
[52] Zepada-Ruis L 2008 Focused ion beams for materials characterization and micromachining *Mater. Res. Soc. Symp. Proc.* **1089E** Y5–2
[53] Pellerin J G, Griffis D P and Russell P E 1990 *J. Vac. Sci. Technol.* B **8** 1945
[54] Vasile M J, Xie J and Nassar R 1999 *J. Vac. Sci. Technol.* B **17** 3085
[55] Barber D J, Frank F C, Moss M, Steeds J W and Tsong I S T 1973 *J. Mater. Sci.* **8** 1030
[56] Carter G, Colligon J S and Nobes M J 1973 *J. Mater. Sci.* **8** 1473
[57] Marzik J V, Croft W J, Staples R J and MoberlyChan W J 2006 Electron microscopy across hard and soft materials *Mater. Res. Soc. Symp. Proc.* **982E** KK7–16
[58] Marshall A F, (laboratory class), Park S I, Marshall A F, Hammond R H, Geballe T H and Talvacchio J 1987 *J. Mater. Res.* **2** 446
[59] MoberlyChan W J, Sanchez E, Stark P and Krug J 2003 *Microscopy* **9** 856
[60] Tiller W A 1991 *The Science of Crystallization* vol II (Cambridge: Cambridge University Press)
[61] Siwy Z and Fuliski A 2002 *Phys. Rev. Lett.* **89** 198103
[62] Gierak J *et al* 2008 Focused ion beams for materials characterization and micromachining *Mater. Res. Soc. Symp. Proc.* **1089E** Y3–1
[63] Davidovitch B, Aziz M J and Brenner M P 2007 *Phys. Rev.* B **76** 205420–1012
[64] Aziz M J 2008 personal communications
[65] Adams D P 2008 personal communications
[66] Adams D P, Vasile M J and Mayer T M 2006 *J. Vac. Sci. Technol.* B **24** 1766
[67] Williams D B and Carter C B 1996 *Transmission Electron Microscopy* (New York: Plenum)
[68] Isabell T C, Fischione P E, O'Keefe C, Guruz M U and Dravid V P 1999 *Microsc. Microanal.* 1999 **5** 126
[69] Adams D P and Vasile M J 2006 *J. Vac. Sci. Technol.* B **24** 836
[70] Zepada-Ruiz L and MoberlyChan W J 2008 in preparation
[71] Notte J *et al* 2006 *SCANNING Proc.* (Mahwah, NJ: FAMS)
[72] Datta A, Wu Y R and Wang Y L 2001 *Phys. Rev.* B **63** 125407
[73] Habenicht S, Bolse W, Lieb K P, Reimann K and Geyer U 1999 *Phys. Rev.* B **60** R2200–3
[74] Stanishevsky A 2001 *Thin Solid Films* **398** 560–5
[75] Biederman H, Slavinska D, Boldyreva H, Lehmberg H, Takaoka G, Matsuo J, Kinpara H and Zemek J 2001 *J. Vac. Sci. Technol.* B **19** 1068
[76] de Wintera D A M and Mulders J J L 2007 *J. Vac. Sci. Technol.* B **25** 2215
[77] Kustner M, Eckstein W, Hechtl E and Roth J 1999 *J. Nucl. Mater.* **265** 22
[78] Facsko S, Bobek T, Stahl A, Kurz H and Dekorsy T 2004 *Phys. Rev.* B **69** 153412
[79] Vogel S and Linz S J 2006 *Europhys. Lett* **76** 884
[80] Harriott L R 1995 *Japan. J. Appl. Phys.* 1 **33** 7094
[81] Habenicht S, Lieb K P, Koch J and Wieck A D 2004 *Phys. Rev.* B **65** 115327
[82] Chan W L and Chason E 2007 *J. Appl Phys.* **101** 121301–46
[83] MoberlyChan W J and Dorsey P 2003 *J. Eur. Ceram. Soc.* **23** 2879
[84] Morimoto H *et al* 1996 *Japan. J. Appl. Phys.* **35** 6623
[85] Morse J, Park H G, Tang V and MoberlyChan W J 2008 *J. Vac. Sci. Technol.* submitted
[86] Dubner A D, Wagner A, Melngailis J and Thompson C V 1991 *J. Appl. Phys.* **70** 665
[87] Young R J and Puretz J 1995 *J. Vac. Sci. Technol.* B **13** 2576